Accepted Manuscript

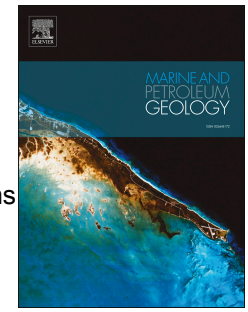

Seismic Geomorphology of Cretaceous Megaslides Offshore Namibia (Orange Basin): Insights into Segmentation and Degradation of Gravity-Driven Linked Systems

Nicola Scarselli, Ken McClay, Chris Elders

PII: S0264-8172(16)30069-1

DOI: 10.1016/j.marpetgeo.2016.03.012

Reference: JMPG 2499

To appear in: *Marine and Petroleum Geology*

Received Date: 29 May 2015

Revised Date: 23 February 2016

Accepted Date: 8 March 2016

Please cite this article as: Scarselli, N., McClay, K., Elders, C., Seismic Geomorphology of Cretaceous Megaslides Offshore Namibia (Orange Basin): Insights into Segmentation and Degradation of Gravity-Driven Linked Systems, *Marine and Petroleum Geology* (2016), doi: 10.1016/j.marpetgeo.2016.03.012.

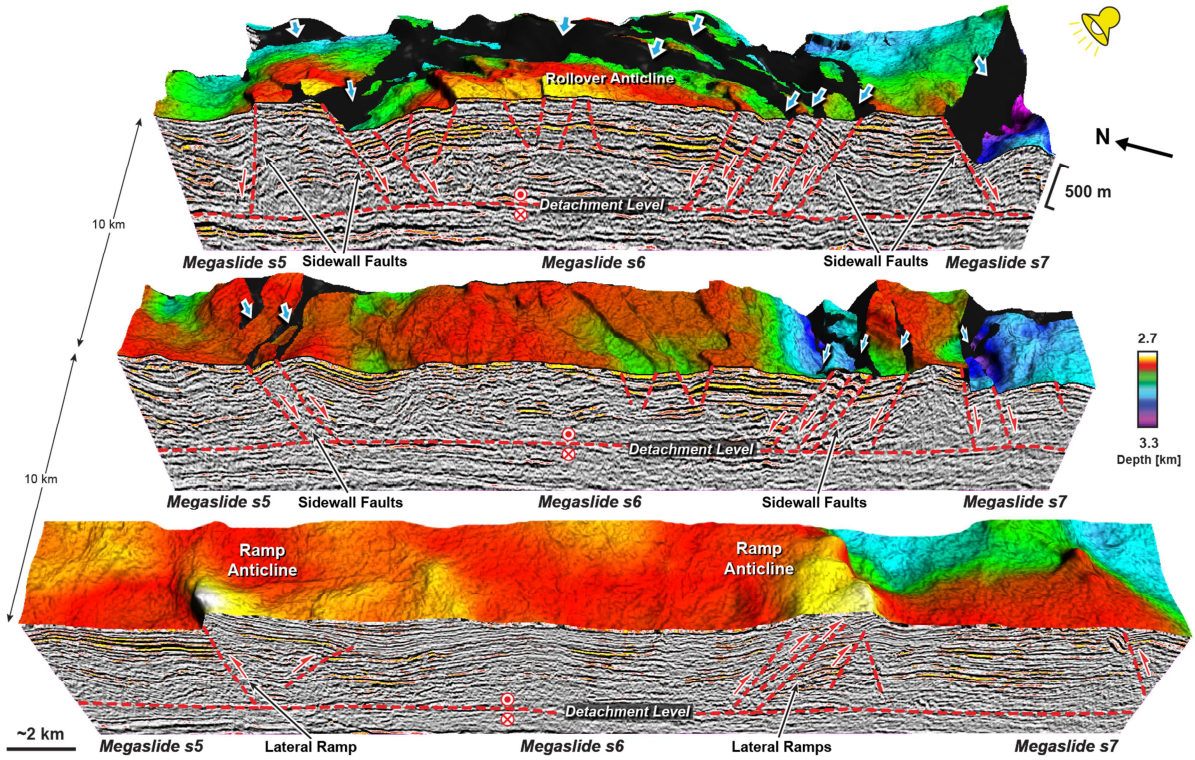

Seismic Geomorphology of Cretaceous Megaslides Offshore Namibia (Orange Basin): Insights into Segmentation and Degradation of Gravity-Driven Linked Systems.

Nicola Scarselli[1*], Ken McClay[1] and Chris Elders[1,2]

1 Fault Dynamics Research Group, Department of Earth Sciences, Royal Holloway University of London, Egham, UK.
2 Now at Department of Applied Geology, Curtin University, Perth, Australia
* Corresponding author: n.scarselli@es.rhul.ac.uk

Abstract
This study applies modern seismic geomorphology techniques to deep-water collapse features in the Orange Basin (Namibian margin, Southwest Africa) in order to provide unprecedented insights into the segmentation and degradation processes of gravity-driven linked systems. The seismic analysis was carried out using a high-quality, depth-migrated 3D volume that images the Upper Cretaceous post-rift succession of the basin, where two buried collapse features with strongly contrasting seismic expression are observed. The lower Megaslide Complex is a typical margin-scale, extensional-contractional gravity-driven linked system that deformed at least 2 km of post-rift section. The complex is laterally segmented into scoop-shaped megaslides up to 20 km wide that extend downdip for distances in excess of 30 km. The megaslides comprise extensional headwall fault systems with associated 3D rollover structures and thrust imbricates at their toes. Lateral segmentation occurs along sidewall fault systems which, in the proximal part of the megaslides, exhibit oblique extensional motion and define horst structures up to 6 km wide between individual megaslides. In the toe areas, reverse slip along these same sidewall faults, creates lateral ramps with hanginwall thrust-related folds up to 2 km wide. Headwall rollover anticlines, sidewall horsts and ramp anticlines may represent novel traps for hydrocarbon exploration on the Namibian margin.
The Megaslide Complex is unconformably overlain by few hundreds of metres of highly contorted strata which define an upper Slump Complex. Combined seismic attributes and detailed seismic facies analysis allowed mapping of headscarps, thrust imbrications and longitudinal shear zones within the Slump Complex that indicate a dominantly downslope movement of a number of coalesced collapse systems. Spatial and stratal relationships between these shallow failures and the underlying megaslides suggest that the Slump Complex was likely triggered by the development of topography created by the activation of the main structural elements of the lower Megaslide Complex. This study reveals that gravity-driven linked systems undergo lateral segmentation during their evolution, and that their upper section can become unstable, favouring the initiation of a number of shallow failures that produce widespread degradation of the underlying megaslide structures. Gravity-driven linked systems along other margins are likely to share similar processes of segmentation and degradation, implying that the megaslide-related, hydrocarbon trapping structures discovered in the Namibian margin may be common elsewhere, making megaslides an attractive element of deep-water exploration along other gravitationally unstable margins.

Keywords: Orange Basin; West Africa; deep-water; gravity-driven deformation, gravity-driven linked systems, slumps, slides, traps

1 Introduction

Gravity-driven processes of deformation have a prime role in shaping the architecture of many continental margins (Butler and Turner, 2010). Margin collapse results from gravity-driven processes acting at different scales producing a wide spectrum of products (Butler and Turner, 2010). Megaslides are margin-scale collapse failures that involve up to 4 km of succession and show a proximal zone of extension connected through a weak detachment surface to a distal contractional domain (Cobbold et al., 2004; Corredor et al., 2005; Damuth, 1994; de Vera et al., 2010; Lawrence et al., 2002; Oliveira et al., 2013; Peel et al., 1995; Roy et al., 2008; Trincardi and Argnani, 1990; Turner, 1995). Collapse is not ascribed to plate tectonics stresses, but it is directly related to the generation of significant gravitational potential on the proximal part of the margin due to high sedimentation rates and phases of uplift (Peel, 2014; Rowan et al., 2004; Schultz-Ela, 2001). For this reason, megaslides are also knows as 'gravity-driven linked systems' (e.g. Rowan et al., 2004) or 'near-field stress-driven linked systems' (Morley et al., 2011).
Although the availability of large amount of 2D regional seismic data along unstable margins has permitted comprehensive studies on the controlling factors and the structural styles of the gravity-driven linked systems (e.g. Lawrence et al. 2002; Rowan et al. 2004; Cobbold et al. 2004; Corredor et al. 2005; de Vera et al. 2010), the intrinsic limits of resolution of 2D seismic data and the scarcity of extensive 3D seismic coverage has limited the understanding of the spatial and temporal evolution of these systems. In particular, little is known about how downdip translation of large sliding masses above a décollement is accommodated laterally. Lateral terminations and internal segmentation of megaslides are thought to occur along oblique slip faults parallel or sub-parallel to the sliding direction (Morley et al., 2011; Stewart, 1999). These features are poorly documented and only few studies, mainly based on 2D data and on 3D volumes with limited coverage, have identified them (Benesh et al., 2014; de Vera et al., 2010; Leduc et al., 2012; Peel et al., 1995; Trincardi and Argnani, 1990). This has resulted in a lack of understanding of how these features fit in the overall evolution of gravity-driven linked systems.

In contrast to gravity-driven linked systems, submarine landslides remobilise and displace only meters to hundreds of meter of sediments, producing mostly incoherent deposits that exhibit a basal shear surface above which material is translated basinward from a proximal headscarp to a distal toe area (Bull et al., 2009; Prior et al., 1984; Richardson et al., 2011). Failure is commonly ascribed to a variety of triggering mechanisms that include slope steepening, seismicity, destabilisation of gas hydrates and high sedimentation rates (Hampton et al., 1996; Judd and Hovland, 2007; Lee et al., 2007; Locat and Lee, 2002; McAdoo et al., 2000). The products of submarine landslides are commonly observed on seismic lines as composite bodies characterised by blocky to highly disrupted and chaotic seismic facies with variable amplitude, which are referred to with a number of terms including, mass-transport complexes, slump complexes, submarine giant landslides or slides (Alves, 2015; Alves and Cartwright, 2010; Bryn et al., 2005; Butler and Turner, 2010; Frey-Martínez et al., 2005; Gamboa et al., 2010; Gee et al., 2007, 2006; Jackson, 2012; Kvalstad et al., 2005; Moscardelli et al., 2006; Moscardelli and Wood, 2008; Posamentier and Martinsen, 2011; Sawyer et al., 2009; Scarselli et al., 2013). Submarine landslides produce numerous structures, some of which may be used as kinematic indicators of their dynamic evolution (sensu Bull et al. 2009). Submarine landslides occur with large scale gravity-driven linked systems (e.g. Trincardi and Argnani 1990; Peel et al. 1995; de Vera et al. 2010) or, together with mass-flows, can be the sole gravity-driven processes active on unstable margins (e.g. Bryn et al., 2005; Frey-Martínez et al., 2005; Pickering and Hiscott, 2015). Whilst previous studies have discussed the morphology and the controlling factors of submarine landslides, less is known about how they interact with large-scale collapse systems (Butler and Turner, 2010; Reis et al., 2010).

This paper presents the results of a 3D seismic case study of two buried collapse features within the Upper Cretaceous succession of the Orange Basin, on the passive margin of Namibia (Fig. 1). During the Late Cretaceous the margin underwent gravitational collapse which produced a large scale gravity-driven linked system (Figs. 2, 3 & 4; de Vera et al. 2010) which, in places, is overlaid by an extensive landslide (Slump Complex in Figure 4). The 3D seismic dataset analysed in this study covers an area large enough to provide a partial image of both the compressional and extensional domain of the gravity-driven linked system and of the overlying submarine landslide. The analysis of this dataset hence provides a unique opportunity to gain insights into the 3D geometries and evolution of gravity-driven linked systems and the extent to which they control the triggering and emplacement of landslides.

2 Regional Overview

The volcanic passive margin of Namibia forms a large continental shelf that extends along the south-west coast of Africa for ~1800 km (Fig. 1a). The margin was developed in response to the stretching of Gondwana since the Late Jurassic, and subsequent opening of the South Atlantic Ocean, between the Nubian and the South American plates, in the Early Cretaceous (Eagles, 2007; Heine et al., 2013; Macdonald et al., 2003; Torsvik et al., 2009). The Walvis Ridge to the north and the Agulhas-Falkland Fracture Zone to the south are two prominent morphotectonic features that define the extent of the margin (Fig. 1a). The Walvis Ridge is a seafloor feature with a relief in excess of 2 km that formed as a hotspot trail associated with the Tristan da Cunha hotspot (Elliott et al., 2009; O'Connor and Duncan, 1990). The impact of this hotspot occurred in the early stages of continental separation and was accompanied by the outpouring of the voluminous Paraná and Etendeka flood basalts (Ewart et al., 1998; Gladczenko et al., 1997; Hawkesworth et al., 1992; Jackson et al., 2000; O'Connor and Duncan, 1990; Peate et al., 1990). The Agulhas-Falkland Fracture Zone is a dextral strike-slip fault zone that accommodated the tectonic separation of the Nubian and the South American plates (Ben-Avraham et al., 1997; Bird, 2001). The Orange Basin is located in the central-southern part of the Namibian margin, opposite the mouth of the Orange River (Fig. 1a), and contains up to 8 km of continental to marine sediments that record the Late Jurassic to present-day rifting and opening of the South Atlantic Ocean (Austin and Uchupi, 1982; Bauer et al., 2000; Brown et al., 1995; Emery et al., 1975; Gerrard and Smith, 1982; Gladczenko et al., 1998; Light et al., 1993; Séranne and Anka, 2005).

3 Tectono-stratigraphy of the Orange Basin

The tectono-stratigraphic history of the Orange Basin was previously investigated using wide-angle seismic surveys and reflection seismic surveys tied to hydrocarbon exploration wells (Austin and Uchupi, 1982; Bauer et al., 2000; Brown et al., 1995; Gerrard and Smith, 1982; Gladczenko et al., 1997; Koopmann et al., 2014; Light et al., 1993; Mello et al., 2011; Paton et al., 2008). These studies identified key reflectors that delimit a number of offshore sequences (Figs. 2 & 3).

3.1 Rift to Post-Rift: Late Jurassic to Aptian

In the Orange Basin, the earliest evidence of crustal stretching and rift deformation is provided by the occurrence of marginal rift basins; NW-SE-trending, isolated grabens and half grabens located beneath the present day inner shelf (Fig. 3; Coward et al., 1999; Gerrard and Smith, 1982; Gladczenko et al., 1998; Jungslager, 1999; Koopmann et al., 2014; Light et al., 1993). Where drilled, these basins contain Upper Jurassic–Lower Cretaceous continental strata and volcaniclastic deposits (e.g. Jungslager, 1999; McMillan, 2003). The Late Jurassic age of these sediments provides the upper constraint for the onset of rifting in the basin (Fig. 3; Gerrard and Smith, 1982; Jungslager, 1999; Light et al., 1993; McMillan, 2003; Séranne and Anka, 2005).

Lithospheric stretching and initial break-up coincided with voluminous volcanic activity as testified by the ubiquitous 'seaward dipping reflectors' (SDRs) observed in the Orange Basin and elsewhere along the Namibian margin (Fig. 2; Bauer et al., 2000; Elliott et al., 2009; Gladczenko et al., 1998; Jackson et al., 2000; Koopmann et al., 2014). SDRs form a series of wedges of volcaniclastic strata, possibly fault bounded (e.g. Fig. 2), emplaced above a stretched and downwarped continental basement (Fig. 3, Gladczenko et al., 1998, 1997).
In the Orange Basin the transition to a passive margin has been generally associated with the Barremian "break-up" unconformity that truncates both the SDRs and the infill of the marginal rift basins and separates these sequences from the overlying Barremian–Aptian sub-parallel strata of Sequence II (Figs. 2 & 3; Brown, 1995; Gerrard and Smith, 1982; Jungslager, 1999; Koopmann et al., 2014; Light et al., 1993; Séranne and Anka, 2005). The onset of "break-up" is in broad agreement with the formation of the ocean magnetic anomaly M4 in the Late Barremian (~126 Ma), which is considered the strongest evidence for the time of opening of the South Atlantic Ocean along the Namibian margin (Eagles, 2007; Heine et al., 2013; Koopmann et al., 2014; Séranne and Anka, 2005; Torsvik et al., 2009).
The Barremian-Aptian Sequence II is regarded as a transitional sequence as it consists of a transgressive succession of terrestrial sandstones intercalated with basaltic lava and overlain by marine sediments (Fig. 3; Gerrard and Smith, 1982; Light et al., 1993; Mello et al., 2011; Séranne and Anka, 2005; Wickens and McLachlan, 1990). Similar transitional sequences have been described elsewhere along the west African margin and indicate that break-up is a process that occurs over a prolonged period of time (Beglinger et al., 2012; Soares et al., 2012; Soares et al., 2014). Sequence II is bounded to the top by Reflector 2, which marks an unconformity of Aptian age (Brown et al., 1995; Gerrard and Smith, 1982; Light et al., 1993). This unconformity is thought to be related to a first phase of post-rift margin uplift (see Section 3.3).

3.2 Post-Rift: Aptian to Present-Day

The marine Aptian to present day post-rift megasequence includes the late Lower Cretaceous Sequence III and the Cenozoic Sequence IV (Figs. 2 & 3, Gerrard and Smith, 1982; Light et al., 1993; McMillan, 2003; Séranne and Anka, 2005). In the lower part of Sequence III, prograding units are bounded by a distinct horizon (Reflector 2a in Figures 2 & 3). These units have been interpreted as ancient shelf edges that developed since the Aptian in response of deepening of the basin and important sediment delivery from the Orange River (Fig. 3; Brown et al., 1995; Gerrard and Smith, 1982; Light et al., 1993; Paton et al., 2008). Well data indicates that in the inner part of the margin Reflector 2a marks an unconformity along which part of the Turonian is missing (Fig. 3; Gerrard and Smith, 1982; Light et al., 1993; McMillan, 2003). This unconformity has been interpreted to be a secondary erosional surface related to the first phase of post-rift margin uplift along the Namibian margin (see Section 3.3). The Turonian strata basinward of the ancient shelf edge have been intersected by commercial wells which found a deep marine succession made up entirely of basinal shales (Light et al., 1993; McMillan, 2003; Wickens and McLachlan, 1990), which has been suggested to form a regional marine source rock unit in the Orange Basin (Aldrich et al., 2003; Kuhlmann et al., 2010). Above Reflector 2a, a succession of Coniacian and younger deep marine shales and silt, occasionally interbedded with sands, has been drilled (Light et al., 1993).
In the continental shelf, Reflector 3 marks an unconformity below which more than 300 m of Maastrichtian to Campanian strata are missing (Fig. 3; Gerrard and Smith, 1982; Hirsch et al., 2010; Light et al., 1993; Paton et al., 2008). The truncation of these strata has been related to the second phase of post-rift margin uplift during the Late Cretaceous (see Section 3.3).
Open-marine sedimentation continued in the Cenozoic into Sequence IV (Figs. 2 & 3). Well cuttings indicate that Sequence IV is made of clays and sands overlain by sandy and shelly limestone and calcareous sandstones (Gerrard and Smith, 1982). Contourite deposits and numerous shallow collapse failures characterise the infill of this sequence (Fig.3; Scarselli, 2014).

3.3 Gravity-Driven Deformation in the Orange Basin

The importance of gravity-driven processes in the evolution of the Orange Basin has been recognised since seminal seismic works carried out along the Namibian margin in the late 70s (Dingle, 1980; Emery et al., 1975; Summerhayes et al., 1979). Later research based on commercial 2D seismic data clearly demonstrated that large megaslide complexes, commonly detached onto Turonian marine shales, have extensively deformed the Cretaceous succession (Fig. 2; Brown, 1995; Butler and Paton, 2010; de Vera et al., 2010; Gerrard and Smith, 1982; Light et al., 1993; Scarselli, 2014. Recent regional mapping of gravity-driven deformation in the Orange basin has shown that almost a third of the volume of the Upper Cretaceous was deformed by a number of these complexes (Scarselli, 2014).
It has been suggested that the failure of the megaslide complexes occurred in the Late Cretaceous, in response to high rates of margin uplift and assisted by a favorably overpressured shale detachment (de Vera et al., 2010). Onset of overpressures within organic-rich shale units due to hydrocarbon generation and resulting reduction of shear strength of shales is a common mechanism for the formation of weak and efficient basal detachments (Cobbold et al., 2009, 2004; Rowan et al., 2004). The occurrence of this mechanism in the Orange Basin seems to be supported by analysis of vitrinite content of the Turonian shale detachment, which indicates that these sediments entered the oil window in the Santonian (~85 Ma) (Hirsch et al., 2010; Kuhlmann et al., 2010).
As reported in Section 3.2, seismic and well data indicate that the Orange Basin experienced a number of phases of uplift in the Cretaceous which are considered to have enhanced gravitational collapse of the post-rift succession (Fig. 3;

de Vera et al., 2010). These pulses of uplift have been corroborated by phases of denudation documented by basin modelling studies and apatite fission track analysis (Fig. 3; Gallagher and Brown, 1999a; Gallagher and Brown, 1999b; Hirsch et al., 2010; Kounov et al., 2009; Raab et al., 2005, 2002; Tinker et al., 2008). The cause of the uplifts remains unknown or subject to debate (Dauteuil et al., 2013; Hirsch et al., 2010; Kounov et al., 2009), with a number of authors suggesting that mantle plume uplifts could have generated vertical stresses at the base of the lithosphere leading to regional topographic uplift (Doucouré and de Wit, 2003; Kounov et al., 2009; Lithgow-Bertelloni and Silver, 1998; Tinker et al., 2008).

4 Seismic Data & Methodology

4.1 Seismic data location and resolution

This study is based on the analysis of 3D depth-migrated marine seismic reflection data. The 3D seismic dataset is located across the present day inner slope of the margin, between water depths of 350 m and 1300 m (Fig. 1b). The dataset has a rectangular shape with dimensions of 35.5 km by 68.1 km and a total area of 2417 km2. Both inlines and crosslines have a shot-point spacing of 25 m and the seismic data is zero-phase reverse polarity with a total penetration of 10 km.

In order to estimate vertical and horizontal seismic resolution, frequency analysis was carried out at a depth interval of 2.5-5 km, which corresponds to the Upper Cretaceous where the collapse features described in this paper are found. The results of the analysis indicated that the dominant frequency within the window of interest is ~15 Hz. Seismic refraction studies in the Orange Basin have indicated that the seismic velocity of the Upper Cretaceous is ~2400 m/s-1 (Bauer et al. 2000). This information suggests that the vertical and horizontal seismic resolution within the section of interest is ~40 and ~80 m, respectively.

4.2 Seismic Attributes

In order to gain insights into the internal and external geometries of the Megaslide Complex and the Slump Complex, stratal slices, depth slices and key horizons have been interpreted (see Section 4.3). Shaded-relief and dip-steered coherency have been extracted along stratal slices and horizons for further in-depth analysis of the two complexes. The two attribute volumes have been generated using dGB OpendTect. Once generated, these volumes have been exported, and together with the amplitude dataset have been analysed using Halliburton geophysical interpretation tools, including Geoprobe and DecisionSpace Desktop.

4.2.1 Shaded Relief

Shaded relief seismic attribute measures the amount of light that variably dipping seismic events would reflect when illuminated by a distant light source (Barnes, 2003). This attribute is designed to display 3D seismic data as illuminated apparent topography when imaged as time slices, thereby aiding interpretation by revealing or suggesting true geology (Barnes, 2010, 2003, 2002). Shaded relief is a directional attribute, therefore features that trend perpendicular to the illumination direction are highlighted, whereas features that trend parallel to that illumination direction are suppressed. For this research shaded relief was calculated following a standard OpenDtect workflow (De Groot and Bril, 2005; Farrukh, 2009). The azimuth of illumination was set to 300º, this value provided the best illumination, perpendicular to the structures analysed in this research.

4.2.2 Dip-Steered Coherency

Coherency is a seismic attribute that measures and compare similarity of adjacent traces (Bahorich and Farmer, 1995; Chopra and Marfurt, 2008, 2007; Marfurt et al., 1998). The attribute highlights discontinuities within seismic data, and it is widely used for detecting faults and changes in seismic facies (e.g. Azar et al., 2009; Iacopini and Butler, 2011). In this research, the generation of the coherency volume has been 'guided' by the local dip of seismic events using a seismic processing method known as dip-steering (De Groot et al., 2004; Marfurt and Alves, 2015). This method provides a dramatic improvement in accuracy and detection power compared to standard coherency (e.g. De Groot et al., 2004). Dip-steered coherency was created following a recommended processing workflow for OpenDtect (Brouwer, 2009; De Groot and Bril, 2005).

4.3 Seismic Interpretation Strategy

Seismic horizons and location of the depth slices analysed in this paper are shown in Figure 4 together with interpreted regional seismic units. Depth-slice at -3450 m is of key significance for the understanding of the 3D geometries of the Megaslide Complex as it cuts both the extensional and contractional domains of the system, revealing how structures evolve in plan view and therefore aiding their full 3D interpretation (Figs. 5 & 6). Horizons P1, K0 and K1 (Fig. 5) mark the main kinematic packages within the Megaslide Complex (see Section 5), allowing timing of structuring of the complex to be inferred. Also, P0 is a bright and continuous pre-kinematic horizon (Fig. 5), that together with K0 and K1 have been displayed in a series of seismic block diagrams in order to show the 3D architecture of the Megaslide Complex (e.g. Figs. 8, 10 & 12).

The basal shear surface of the Slump Complex has been used to define its shape and regional extent (Fig.13). The basal shear surface and top of the Slump Complex have been mathematically combined to generate a proportional slice (sensu Posamentier et al. 2007) within the complex (see Figure 4 for its location). Along the proportional slice and key depth-slices, coherency and amplitude have been co-rendered and co-displayed (sensu Posamentier et al. 2007). This allowed

unravelling of the internal seismic facies arrangement of the complex (Fig. 13). Exploded seismic block diagrams are also shown in order to present the lateral variations of the internal geometry of the upper Slump Complex as well as to elucidate the relationships of these variations with the structures forming the underlying Megaslide Complex (e.g. Figs 19 & 20).

5 Seismic Stratigraphy

Figure 4 shows the seismic characteristics of a key dip section through the 3D dataset. The Megaslide Complex and the Slump Complex occur within the Aptian-Maastrichtian Sequence III. The seismic stratigraphic framework for the two complexes is presented below.

5.1 Stratigraphy of the Megaslide Complex

5.1.1 Basal Detachment

The Megaslide Complex is characterized by updip (to the NE) listric extensional growth faults and downdip (to the SW) basinward-vergent imbricate thrust faults that sole out onto a common detachment level (Fig. 4). Based on seismic stratal relationships and published well and seismic data, the strata forming the detachment level are ascribed to the Turonian marine shales (de Vera et al., 2010; Scarselli, 2014). These shales are seismically characterised by a discontinuous facies with variable amplitude (Fig. 4). The detachment is a strikingly sub-horizontal surface that typically displays subtle ramps that possibly link multiple levels of basal slip at different stratigraphic levels (Fig. 4). Above the detachment, a section of up to 2 km of Upper Cretaceous strata has been involved in the emplacement of the Megaslide Complex (Fig. 4). Based on stratal-structural relationships shown in Figure 4 and detailed in Section 6, this section has been divided into four main kinematic units. From older to younger these units are: Pre-Kinematic, Syn-Kinematic I, Post-Kinematic I and Syn-Kinematic II (Fig. 4).

5.1.2 Pre-Kinematic Unit

This section is formed by a package of relatively continuous reflections and is bounded to the bottom by the detachment level and to the top by horizon P1. The unit is deformed by faults and folds and does not contain growth strata, indicating that its deposition pre-dates the activation of these structures. The basal part of the section is poorly imaged and seems to comprise a ~200 m thick package of disrupted reflections that may represent a slump unit (e.g. Figs. 4 & 7). Along this part of the margin early slump events have been commonly observed within the Cenomanian-Turonian section, and these have been ascribed to an earlier stage of margin collapse (Scarselli, 2014).

5.1.3 Syn-Kinematic Unit I

This unit is characterised by mostly continuous seismic reflections with variable amplitudes and is bounded to the bottom and to the top by horizons P1 and K0, respectively. The section contains clear growth strata associated with the development of the thrusts faults forming the contractional domain (e.g. Figs. 4 & 11), indicating that the its deposition was coeval with the activation of these structures.

5.1.4 Post-Kinematic Unit

This unit is formed by a package of high amplitude, relatively continuous reflections up to 300 m thick that is bounded by horizon K0 to the bottom and horizon K1 to the top. The section does not exhibit any growth geometries associated with the thrust and extensional faults that displace it, indicating a time of limited fault activity (e.g. Figs. 4, 7 & 11).

5.1.5 Syn-Kinematic Unit II

This unit comprises a package of mostly low amplitude, continuous reflections bounded at the base by horizon K1, with the upper section of the unit heavily eroded by the basal shear surface of the overlying Slump Complex (Fig. 4). The unit exhibits clear growth strata associated with the extensional faults (e.g. Figs. 4 & 7), indicating that its deposition occurred together with structural activity along those faults. However, there is no evidence of syn-kinematic sequences associated with the thrust fault within this package, indicating that extension and contraction in the Megaslide Complex were not coeval. The implications of this apparent dichotomy are presented in Section 6.4 and discussed in Section 9.

5.2 The Slump Complex

A high amplitude and irregular eroded surface marks the basal shear surface of the overlying Slump Complex (Fig. 4). The complex has a highly variable thickness ranging from a few meters up to 800 m (Fig. 4). As detailed in Section 7, the system is characterized by a number of seismic facies consisting of chaotic, disrupted to semi-continuous reflections. The top of the Slump Complex is defined by a high to low amplitude, mostly continuous reflection which separates it from the overlying uppermost Upper Cretaceous to Present-day succession (Fig. 4).

6 Megaslide Complex

The structural architecture of the Megaslide Complex is illustrated in the coherency and shaded relief depth slices shown in Figure 5. These reveal prominent E-W trending faults that divide the complex into three main segments: the

northern megaslide s5, the central megaslide s6 and the southern megaslide s7. Megalides s5 and s7 are only partially covered by the 3D survey whereas the width of the central s6 is entirely imaged (Fig. 5). Central megaslide 6 is approximately 20 km wide and at least 30 km long (Fig. 5). The length of the megaslide is likely to be much longer as the contractional and extensional domains are not imaged in full, and regional 2D mapping has shown multiple rotated extensional fault blocks updip of the ones observed in the 3D dataset (Scarselli, 2014). The central megaslide s6 is clearly defined by three main fault systems: (1) a N-S- trending headwall fault system, (2) an E-W-trending sidewall fault system and (3) a N-S trending thrust fault system. The structures forming these domains have been mapped in detail and are illustrated in the 3D fault model of megaslide s6 shown in Figure 6.

6.1 Headwall fault system

Basinward-dipping, N-S-trending, listric extensional faults arranged in a spoon-shaped geometry form the headwall fault system (Figs.5-7). Spacing between adjacent faults is 0.5-1.5 km, with an overall fault length of 10-15 km (Fig. 7). Fault displacement and fault dip vary from 50-400 m and 40°-20° respectively (Fig. 7) The fault system delineates a series of tilted fault blocks that commonly show pronounced rotation, reaching values in excess of 30º (Fig. 7). Lower fault dips, larger displacements and a higher degree of block rotation seem to be associated with the more external (i.e. landward) faults (Fig. 7), possibly indicating an overall basinward migration of extensional strain within the system. Within the fault blocks, syn-extension sedimentation is revealed above horizon K1 by wedge-shaped growth strata of the Syn-Kinematic II unit that exhibit thickening and fanning against adjacent fault planes (Fig. 7). Growth strata within highly rotated fault blocks can attain thicknesses of ~1 km (Fig. 7).

Laterally the faults curve towards their tips and link with the sidewall fault systems forming the typical spoon-shaped arrangement of the headwall system (Figs. 5 & 6). As the headwall strata dip into these arcuate arrays of faults, they form a prominent, dome-shaped 3D rollover anticline (Fig. 8). The anticline is ~20 km across and is typically affected by crestal collapse features that occur in the form of closely spaced normal faults and horst & graben structures (Figs. 8, 9a & 10a).

6.2 Sidewall fault system

The sidewall fault system consists of opposite dipping, arcuate, E-W-trending faults that laterally divide the megaslides and consistently offset, and thus post date, the structures forming the N-S trending thrust fault system (Fig. 5). In the headwall area the sidewall systems are formed by sets of normal faults with dips of ~30º and typical displacements of ~400 m (Fig. 9a). Between adjacent megaslides, the fault systems form pronounced sidewall horsts up to 6 km wide that extend basinwards for 10-15 km (Fig. 10a & b). Clear fanning of dips above horizon K1 is observed in the hanging wall of this proximal segment of the sidewall faults (Fig. 9a), indicating coeval development of these structures with the headwall faults.

Downdip of the headwall area the displacement of the sidewall faults reduces and structural complexity increases, as shown by the occurrence of potential thrust anticlines reactivated in extension and fault splays which exhibit reverse movement along their slip surfaces (Fig. 9b). A component of oblique slip may be increasingly important along this segment of the sidewall faults.

Towards the toe area, the sidewall faults change progressively to clear reverse faults with dips of 40º-50º and typical displacements in excess of 400 m (Fig. 9c). The reverse faults together with well imaged associated hanging wall folds form prominent lateral thrust ramps and anticlines up to 2 km wide that laterally bound the toe region of the megaslides (Figs. 9c & 10c). The deep erosion of the Slump Complex above the ramp anticlines of the central megaslide hinders a clear identification of the associated growth strata (Fig. 9c). This prevents any inference of the precise timing of the activation of these structures. Nevertheless, thrusting along the lateral ramps has clearly affected horizon K1 (Fig. 9c), indicating that these ramps developed together with, or shortly after, the headwall faults.

6.3 Thrust fault system

A series of N-S-trending landward-dipping imbricate thrust faults with associated basinward verging, asymmetric hanging wall folds form the thrust fault system (Figs. 4, 6 & 11). Thrust faults spacing and fault ramp geometries vary greatly along strike, with ramp angle of 30°-40° and hanging wall folds up to 3 km across (Figs. 4 & 11). Identification of growth strata associated with the thrust fault-related folds is possible only in selected parts of the survey where the emplacement of the Slump Complex has not completely obliterated the underlying section (Fig. 11). Syn-thrust sedimentation above horizon P1 is evidenced by packages of reflections of the Syn-Kinematic I unit that onlap onto the fold limbs and exhibit fanning geometry (Fig. 11). These growth strata are generally thin, with maximum thicknesses of ~200 m found in the backlimb of the folds (Fig. 11).

The thrust fault system exhibits master fault segments that extend laterally for tens of kilometres (Fig. 5). From these, minor km long segments branch off, together creating a complex fault network that is displaced by the distal segments of the E-W-trending sidewall faults (Fig. 5). In this complex setting, fault spacing is highly variable and as it decreases, the interaction between contiguous thrust ramps becomes increasingly important in shaping the style of the system (Fig. 12). This is readily seen by the fact that fault shape of inner (to the NE) thrust ramps gradually changes from sigmoidal to listric when the distance from contiguous ramps decrease below ~2 km (see the along strike evolution of fault T2 in Figure 12). The geometry of the hanging wall folds changes consistently with the shape of the associated thrust ramps. This is evidenced by the fact that sigmoidal thrust ramps typically exhibit hanging wall folds with a well developed narrow and steep forelimbs (see fold F1 in Fig. 12), whereas folds in the hanging wall of listric thrust faults typically

have gentle forelimbs (see F2 in Fig. 12c) or flat crests (see F3 and F4 in Fig. 12), and commonly exhibit parasitic folds at the associated thrust tips (e.g. see F2 in Figure 12c).
The observations above suggest that the thrust fault system developed in a forward-breaking sequence, thus emplacement of outer, younger thrusts caused back rotation and straightening of inner, older thrust ramps together with refolding and flattening of the forelimbs of the associated hanging wall folds.

6.4 Timing of Headwall Extension and Toe Contraction

Analysis of kinematic strata described above (Figs. 7, 9 & 11) together with the fact that the thrust systems were displaced by the sidewall faults (Fig. 5) strongly suggests that the structuring of the headwall and sidewall systems was coeval and postdates the build-up of the fold and thrust belt. Key sections also show that the Syn-Kinematic I unit and the Syn-Kinematic II unit are divided by a 300 m thick package of parallel reflections of the Post-Kinematic I unit (Fig. 11). This observation indicates that, after the build-up of the fold and thrust belt, a significant amount of time elapsed before the activation of the coeval headwall and sidewall fault systems. The striking mismatch between the timing of headwall extension and toe contraction implies episodic structuring of the megaslides through two successive sliding events separated by a phase of quiescence. As discussed in Section 9, it is suggested that the extension associated with the first phase of sliding took place outside and updip of the study area and deformation shifted basinward during the second phase of sliding. Basinward shift of deformation is independently supported by patterns of basinward propagation of strain as observed in the extensional and contraction domains. Local gentle folding of the Post-Kinematic I and Syn-Kinematic II units above the thrust faults (Fig. 11), also suggests that the fold and thrust belt may have experienced a secondary phases of activity, likely related to the activation of the extensional faults at the headwall during the second sliding event.

7 Slump Complex

The Slump Complex is seismically characterised by a disrupted to chaotic facies with the basal shear surface that clearly cuts into the lower Megaslide Complex at different stratigraphic levels (Fig. 4) The 3D dataset clearly images the northern and southern flanks of the Slump Complex, but not the updip (to the E) and downdip (to the W) terminations of the system (Fig. 13a). Thus it is only in the central part of the complex where mapping of the basal shear surface and seismic facies analysis were carried out (Fig. 13). Regional 2D seismic mapping has indicated that the system extends over an area ~1200 km2 with a total runout of in excess of 50 km and a volume of ~600 km3 (Scarselli, 2014).

7.1 Seismic Facies Analysis

The internal seismic expression of the Slump Complex is revealed by a co-rendered amplitude-coherency extraction along the proportional slice halfway between its basal shear surface and top surface (Fig. 13b). Although the complex is largely characterised by a strongly disrupted seismic facies, careful examination of the extraction allows recognition of distinct seismic signatures and deformational geometries. Two main seismic facies associations are defined, these are (1) a coherent facies made of blocks of relatively continuous reflections with a very discontinuous to transparent seismic facies in between and (2) an overall highly disrupted to chaotic seismic facies.

7.1.1 Coherent Blocks and Associated Transparent Seismic Facies

This facies association is observed in limited areas in the northern and southern part of the Slump Complex (Fig. 13b). As detailed below, the coherent facies represents a series of blocks of variable dimensions that have been evacuated by well defined headscarps. These blocks are labelled Slide Block N, Slide Block S and Slide Block NE in Figure 13c.

Slide Block N

The northern flank of the Slump Complex exhibits three distinct areas characterised by coherent seismic facies (Figs. 13b & 14) that form three blocks of relatively intact stratigraphy (Slide Block N1, N2 & N3 in Figures 14 & 15). The three slide blocks are part of a large complex labelled Slide Block N in Figure 13c.
The blocks are characterised by high to low amplitude, continuous reflections, with dips in excess of 30º abutting against the basal shear surface, indicating that these blocks represent portions of stratigraphy that have slid and rotated during emplacement–slide blocks (Fig. 15). The headscarps bounding the blocks form arcuate segments in planform which extend for over 10 km (Fig. 14), and in vertical section appear as surfaces that sole out at the basal shear surface with a planar to listric shape, reaching dips up to ~40° (Fig. 15). The headscarps propagate upward affecting some 600 m of post-slumping strata, suggesting that they were reactivated as normal faults after that failure occurred (Fig. 15). With lengths up to 12 km and widths up to 4 km, the blocks are markedly elongated and can attain heights of ~500 m, with volumes of individual blocks in excess of 10 km3 (Figs. 14 & 15). The distance between adjacent blocks indicates that these slid above the basal shear surface for hundreds of meters (Fig. 15). Also, their irregular cross sectional shape, pervasive internal faulting and conspicuous stratal erosion at their top surfaces, suggest that the blocks are severely degraded, a further indication of their downslope transport (Fig. 15). The arcuate planform of the associated headscarps (Fig. 14) may imply that the blocks were deformed by loading of material evacuated by subsequent headscarp collapses. This, in turn, would suggest an overall component of retrogradation in the development of the complex.

The coherent and continuous facies that characterised the blocks is significantly different to the very discontinuous, transparent to low amplitude seismic facies that occur between them (Figs. 14 & 15). This facies with no internal reflectivity typifies the presence between the blocks of deposits with no stratal organization. These considerations may indicate that the transparent facies represent mass flows that where generated by the degradation of the slide blocks and that infilled the accommodation created by the evacuation of the blocks (Fig. 14).
Slide Block N is bounded downdip by a series of E-W-trending, closely spaced, north-verging thrusts (Fig. 16). These can be likely interpreted as 'thrusts in the terminal wall' (sensu Posamentier and Martinsen, 2011) that developed as the Slump Complex terminated laterally above the underlying northern lateral ramp of megaslide s6 (Fig. 16).

Slide Block S & NE

The Slide Block S and Slide Block NE are located in the southern and northeastern part of the Slump Complex respectively (Figs. 13b & c). Slide Block S comprises two blocks up to 4 km across that were evacuated by a common, linear headscarp that defines the southern flank of the Slump Complex (Fig. 13c). By contrast Slide Block NE forms a spoon-shaped, headwall scarp up to 10 km across that imparts a relief of ~500 m along the basal shear surface of the complex (Figs. 13a & c).

7.1.2 Chaotic Seismic Facies

Large extents of the Slump Complex exhibit a low coherency, disrupted seismic facies with variable amplitude (Figs. 13b & c). Within these areas, distinct subunits, which are termed slump lobes, can be tentatively identified, suggesting that this large disrupted mass is the combination of several coalesced collapse features (Fig. 13c). The slump lobes are presented below together with the evidence that support their identification.

Slump Lobe CS, CN & S

These lobes are located in the central-southern part of the Slump Complex (Figs. 13b & c). The lobes are laterally defined by SE-NW-trending lineations–parallel to the transport direction– marked by semi-continuous reflections with variable amplitude that are clearly imaged on depth slices as well as proportional slices (Figs. 13b & 17). These lineaments are interpreted to be longitudinal shear surfaces (sensu Bull et al., 2009), heavily sheared bands that form between adjacent failures segments evolving at different strain rates. The longitudinal shear surfaces that bound Slump Lobe CS constrain transverse, arc-like strings of semi-continuous reflections (Fig. 17). Dip sections through these features shows packages of continuous reflections steeply dipping to the east (Fig. 18). Given the gross transport direction towards west, these can be tentatively interpreted either as thrusts or, similarly to Slide Block N, evacuated blocks that have deformed by loading of material sourced upslope (Fig. 18). A scoop-shaped scour up to 2 km across is observed at the basal shear surface immediately beneath these continuous, tilted packages (Figs. 13a, b & c). This feature may be tentatively interpreted as the relic of a headscarp that has been overflowed by successive slump events sourced further upslope (i.e. to the east; Fig. 13c, see also mega scour in Fig. 19a). In this view the continuous and tilted packages of reflections would constitute heavily deformed slide blocks rather than thrusts. Irrespective of the interpretation, the spatial association of longitudinal shears and these packages of more continuous strata supports the occurrence of multiple failure segments within the heavily disrupted component of the Slump Complex (Fig. 13c).
Slump Lobe S is located between the Slide Block S to the south and the Slump Lobe CS to the north (Figs. 13b & c). The upslope termination of the lobe is not clear as it is located at the southern limit of the 3D dataset (Figs. 13b & c). It is likely that the proximal part of this unit extends further to the SE, with the slump having a different source area with respect to the other lobes (Fig. 13c). The downdip toe of the lobe is partly imaged in the 3D data and exhibits a prominent basal ramp with associated west-verging thrusts terminating above the southern lateral ramp of underlying megaslides s6 and s7. (Figs. 13c & 19a).
Slump Lobe CN is bounded to the north by the Slide Block N and to the south by the Slump Lobe CS (Fig. 13c). The upslope termination of the lobe is not clear and, similarly to Slump Lobe CS, it may have been obliterated by the collapse of lobes sourced further updip (Fig. 13c).

Slump Lobe NE and Lobe SE

The chaotic mass in the eastern (i.e. proximal) part of the Slump Complex can be tentatively divided into Slump Lobe NE to the north and Slump Lobe SE to the south (Fig. 13c). These units are defined on the base of two adjacent, km-wide, basal scours (Figs. 13a & c) that cut deeply into the underlying Megaslide Complex (see mega scours in Fig. 20). The source area of these units is likely located further to the E, in an area not imaged by the 3D data. Regional 2D mapping further updip shows listric headscarps, up to 500 m in height, that cut into the footwall of major normal faults of the underlying Megaslide Complex (Scarselli, 2014). These may be the headscarps associated with these slumps. The Slump Lobe SE likely merged downdip with Slump Lobe CN, CS and S forming a continuous contorted irregular deposit (Figs. 19a & b), whereas the downdip segment of Slump Lobe NE was obliterated by the late emplacement of the Slide Blocks NE and N (Figs. 13c, 19c & 20).

8 Slump Complex – Megaslide Complex Relationships

Several observations can be made on the control of the lower Megaslide Complex on the emplacement of the upper Slump Complex and on the timing of emplacement of the two complexes.

8.1 Timing of Megaslide & Slump Complex Emplacement

The collapse of the Slump Complex resulted in erosion and deformation at multiple levels of the kinematic stratigraphy of the underlying Megaslide Complex (e.g. Figs. 4 & 11). Therefore, the identification of the kinematic packages that were affected by the collapse of the Slump Complex provides a broad constraint on the timing of the emplacement of this system with respect to the structuring of the underlying megaslides.

As described in Section 6.4, the development of the Megaslide Complex occurred through the activation of the various fault systems at different times. In particular it has been noted that thrusting was followed by a phase of quiescence before the onset of the structuring of the headwall and sidewall systems. This phase of quiescence is revealed by a package of parallel reflections of the Post-Kinematic unit that seal the underlying growth strata associated with the thrust faults (Fig. 11). In places this post-thrust unit is clearly not affected by the Slump Complex (Fig. 11). This indicates that a considerable span of time separated the formation of the thrust fault system and the collapse of the Slump Complex. Given the thickness of the post-thrust unit of ~200 m and assuming a typical slope sedimentation rate of 10–50 mMyr-1 (Middleton, 2003), the emplacement of the Slump Complex post dates the fold and thrust belt of the Megaslide Complex by several millions of years. In contrast, the Slump Complex everywhere cuts into the syn-kinematic packages associated with the headwall and sidewall faults of the Megaslide Complex (e.g. Figs. 4, 7 & 9a), suggesting that its emplacement may have occurred during or shortly after the activation of those fault systems.

8.2 Megaslide Complex Control on Slump Complex Morphology

The potential constrains of the lower Megaslide Complex on the morphology of the upper Slump Complex are explored with Figure 13d that shows the superposition of the structures of the two complexes. The map clearly shows that the major structural elements of megaslides s6 and s7 broadly constrained the lateral extent of the overlying Slump Complex (Fig. 13d).

8.2.1 Control of the Sidewall Structures

The northern and southern flanks of the Slump Complex seem to be constrained by the E-W-trending sidewall fault systems that bound megaslides s6 and s7 (Fig. 13d). This is readily seen in particular along the northern flank of the Slump Complex, where large headscarps of Slide Block N correspond to the position of the extensional segment of the underlying sidewall faults of megaslide s6 (Fig. 13d), whereas, further west, where the sidewall fault system has a distinct reverse slip, the basal shear surface of the Slump Complex ramps up stratigraphy and the complex terminates above the ramp anticline of the underlying central megaslide 6 (Figs. 13d & 16). This suggests that the relief created by the northern ramp anticline of the megaslide acted as a barrier for the advance of the slump masses.

To the south the relationships between the two complexes are not as obvious; however, similarly to observations to the north, the basal shear of the Slump Complex ramps up stratigraphy and the complex terminates with a series of thrusts above the lateral ramps of megaslides s6 and s7 (Figs. 13c & 19a). This further corroborates the interpretation that the lateral ramps at the toe of underlying megaslides formed high relief areas at the time of the downslope collapse of the Slump Complex.

8.2.2 Control of the Headwall Structures

The structural elements at the headwall of the megaslides also strongly controlled the morphology of the Slump Complex. This is indicated by the fact that headscarps of Slide Block NE have developed along the uppermost segments of the scoop-shaped headwall faults that delineate the rollover anticline of megaslide 6 (Fig. 20b). This may suggest that the headwall megaslide structures formed weak zones which were exploited by Slide Block NE, imparting to it a markedly arcuate planform geometry (Fig. 20b).

Also, Slump Lobe NE and Slump Lobe SE noticeably thin towards the structural highs at the headwall of the underlying megaslides. This is shown by the reduced thicknesses of these lobes above the rollover anticline of megaslide s6 and above the sidewall horsts that laterally bound the megaslides (Fig. 20). Thinning of the slump lobes above these structurally controlled morphological barriers suggests that the collapse of the Slump Complex was coeval or shortly after the activation of the headwall structures of the megaslides.

8.2.3 Control of the Thrust Fault System

The morphology the basal shear surface of the Slump Complex above the thrust fault system of the central megaslide 6 the is strikingly flat (Figs. 19b & c). This may suggest that the collapse of the Slump Complex in this area occurred above a featureless morphology as the thrust fault system was sealed by a considerable thickness of flat post-thrusting strata. This, in turn, indicates that the imbricates did not control the development of the overlying Slump Complex.

9 Discussion

A model for the evolution of the Namibian Megaslide Complex is proposed in Figure 21. The model also illustrates the relationships between the Megaslide Complex and the Slump Complex, contributing to previous discussions regarding the control of the structuring of gravity-driven linked systems on the initiation and emplacement of submarine landslides (Butler and Turner, 2010; Reis et al., 2010).

9.1 Segmentation and Evolution of the Megaslide Complex

Structuring and segmentation of the Namibian Megaslide Complex are discussed in the following sections. The evolutionary path presented is compared to sandbox experiments and natural examples to asses the wider applicability of the model proposed.

9.1.1 Model for Structuring of Megaslides

The emplacement of the Megaslide Complex occurred episodically through multiple sliding events (Fig. 21). A first stage of margin instability triggered the onset of early megaslides in the proximal part of the margin (Fig. 21a). The extent of the 3D data available for this research did not allow imaging of the extensional domain of these early systems, which are likely located updip of area analysed. Upslope of the study area, regional 2D seismic lines have shown the occurrence of a number of seaward-dipping listric faults bounding markedly rotated fault blocks up to 7 km wide (de Vera et al., 2010; Scarselli, 2014). These may represent the extensional counterpart of the well imaged fold and thrust belt shown in this study.

A period of quiescence followed the emplacement of the proximal megaslides (Fig. 21b). During this period early structures were deactivated and buried (Fig. 21b). Renewed margin instability brought about a basinward shift of sliding with the formation of spoon-shaped headwalls that have been described in this study (Fig. 21c). Translation of material away from the headwalls of the megaslides was laterally accommodated by oblique extensional motion along the proximal part of the sidewall fault systems (Fig. 21c). As translation progressed downslope, rotation of strata into the headwall faults as well as into the sidewall faults created prominent headwall rollover anticlines together with sidewall horsts bounding adjacent megaslides (Fig. 21c). Early structures were displaced by the sidewall faults and transported downslope by the newly emplaced megaslides (Fig. 21c). Downdip and lateral spreading of the failing mass induced mild reactivation of early thrust faults and the onset of reverse slip along the distal segment of the sidewall systems, which, in turn, resulted in the formation of lateral ramps and associated anticlines (Fig. 21c). Newly formed thrust faults are expected to be present downdip of the study area as these would have accommodated this later stage of sliding (Fig. 21c). Partially imaged, well-structured thrust ramps are observed at the westernmost limit of the 3D data (Fig. 4), suggesting that the contractional domain of the Megaslide Complex extends well outside the study area, and such thrust ramps are likely present further downslope.

9.1.2 Mechanisms for Episodic Basinward Development & Segmentation of Megaslides

Initiation of gravity-driven linked systems has been ascribed to three main mechanisms (1) gravity spreading sustained by sediment progradation, (2) gravity gliding driven by progressive tilt of the detachment and (3) a combination of the two (e.g. Peel, 2014; Rowan et al., 2004; Vendeville, 2005). In this work, high quality, depth migrated 3D seismic has clearly shown that the extensional and contractional domains of the megaslides are located above a striking subhorizontal basal detachment (Fig. 4), implying that the Cretaceous phases of uplift did not result into marked basinward tilting of the part of the margin analysed in this study. This therefore, indicates that gravity gliding had limited contribution into driving the collapse of the Namibian megaslides, whereas gravity spreading, sustained by sediment discharge from the Orange River since the Aptian, may have been key in the development of these systems. The distinct episodic behaviour of emplacement of the Namibian Megaslide Complex are likely related to phases of activation and deactivation of the mechanisms that assisted sliding such as, surges of sediment delivery to the basin and pulses in generation and dissipation of overpressures within the Turonian detachment. Theoretical models for gravity spreading have predicted a temporal link between episodes of basinal deposition with phases of gravity deformation (Peel 2014). The results of these models, together with the fact that accumulation rates in the Late Cretaceous Orange Basin were high and variable (Guillocheau et al., 2012; Rust and Summerfield, 1990), suggest a strong control of sedimentation on the episodic emplacement of the Namibian megaslides.

The lateral extent of these driving mechanisms is likely to have controlled the distribution and size of the Namibian megaslides. Lateral changes in the physical properties of the Turonian shales forming the basal detachment of the megaslides may have been responsible for uneven distributions of overpressures. This in turn may have led to lateral variations in the efficiency of the detachment, favouring formation of distinct segments of failure. On the other hand, localised and persistent deposition of discrete lobes of sediments may have created thick and unstable sediment wedges that underwent gravitational collapse. It is suggested that with sustained delivery of sediments, new unstable wedges would develop basinward, driving a downslope propagation of segmented megaslides. The latter mechanism again highlights the importance of sedimentation and gravity spreading over gravity gliding for the emplacement of the Namibian megaslides as compared to the conclusions of other authors (de Vera et al., 2010; Peel, 2014).

The segmentation into distinct units of collapse of the Namibian Megaslide Complex shares similarities with the “multi-cell model” for the development of slumps that has recently been proposed by Alsop and Marco (2014). The authors analysed in detail well exposed outcrops of slumped units within the late Pleistocene Lisan Formation of the Dead Sea basin. They recognised that the slumps are composed of several small, second-order flow cells (i.e. slump failures) driven by laterally restricted, second-order perturbations, such as local variations in lithology, fluid pressure and slope steepness. This suggests that segmentation occurs at all scales in all types of gravity-driven processes of deformation.

9.1.3 Comparisons with Sandbox Experiments & Natural Examples

Lateral segmentation and basinward shifting of slides are also observed in analogue models (e.g. Mourgues and Cobbold 2006; Mourgues et al. 2009). In those models, sand wedges were successively layered on a rig where

compressed air was injected at its base, so that to simulate deformation driven by sediment progradation above overpressured shale detachments. Top views of the model rig have shown the occurrence of progressively overlapping slide units with long fractures that laterally bound and link the contractional and extensional domains of the sliding sand pack (Mourgues et al., 2009). It is very likely that those fractures accommodated the progressive evolution of the sliding sand pack, hence they can be favorably compared with the sidewall faults presented in this research. This leads to the conclusion that the lateral segmentation of the Namibian Megaslide Complex into distinct units represents an important benchmark for sand box models of gravitational sliding above overpressured detachments.

The characteristic features that typify the lateral segmentation of the Namibian Megaslide Complex are not unique to this system. Regional 2D seismic interpretation offshore the Amazonas Fan, in the Brazilian Equatorial passive margin, has permitted extensive mapping of the late Miocene, shale-rooted, Amazonas gravity-driven linked system (Reis et al., 2010). Structural maps of a section of the margin ~200 km long shows an extensional domain located in the shelf-upper slope and a contractional domain in the slope setting of the basin. The maps clearly illustrate adjacent arrays of updip extensional faults and downdip thrust consistently segmented into adjacent zones of deformation up to 60 km across. The laterally discontinuous arrangement observed in the structural domains of the Amazonas system may reflect similar segmentation of the megaslides to that observed in the Namibian margin (Fig. 20). Lateral partitioning has also been reported to characterise a number of prolific gravity-driven fold belts, such as those offshore Mozambique (Law, 2011), Niger Delta (Benesh et al., 2014; Leduc et al., 2012) and Gulf of Mexico (Peel et al., 1995). This suggests that the model of lateral segmentation of megaslide complexes proposed in this study may have wide applicability. This, in turn, implies that the potential novel structural traps presented in this study, such as lateral thrust ramps, sidewall ridges and rollover anticlines, may be common elsewhere, making megaslides a more attractive element of deep-water exploration along gravitationally unstable margins.

Previous studies of gravity-driven linked systems also show that they share many similarities with subaerial landslides (e.g. Damuth 1994; de Vera et al. 2010), a conclusion supported by this research. The Namibian megaslides clearly show extensional headwalls laterally delimited by sidewall faults and sidewall ridges with contractional folds at their toes. Similar features such as 'strike-slip faults' that laterally divide subaerial landslides have been readily observed and mapped in detail in a number of studies (e.g. Fleming and Johnson, 1989; Parise, 2003).

9.2 Slump Complex Emplacement & Degradation of the Megaslide Complex

Seismic evidence shows that Slump Complex cut deeply into the syn-kinematic strata of headwall and sidewall structures of the underlying Megaslide Complex. This indicates that emplacement of the Slump Complex was controlled by the structuring and segmentation of the underlying Megaslide Complex, causing widespread degradation of the shallow section of the latter (Fig. 21d). Triggering mechanisms and wider implications of the degradation of the megaslides are discussed.

9.2.1 Triggering Mechanisms and Emplacement

A number of triggering factors have been proposed for the collapse of submarine landslides worldwide (Hampton et al., 1996; Lee et al., 2007; Locat and Lee, 2002). Because the Slump Complex is largely controlled by the structuring of the underlying megaslides, it is suggested that relevant triggering mechanisms should be sought amongst those related to fault activity. Commonly these are limited to three (1) slope steepening, (2) fluid seepage and (3) seismic shaking (Gee et al., 2006; Hampton et al., 1996; Lee et al., 2007; Locat and Lee, 2002). Although this study did not provide compelling evidence for assessing the effectiveness of the three triggering factors, these are broadly evaluated in the context of this study.

Gravity exerts a downslope driving stress, and an increase of slope steepness due to faulting can lead to slope instability (Gee et al., 2006; McAdoo et al., 2000; Morley, 2009; Moscardelli and Wood, 2008). The Statfjord Field slide system, offshore Norway, is an example of submarine landslides triggered by fault-related slope steepening (Hesthammer and Fossen, 1999; Welbon et al., 2007). The system collapsed as a result of the activation of regional extensional faults which created high relief areas along the elevated footwall of those structures (Hesthammer and Fossen, 1999). Similarly, the structuring of the Namibian megaslides may have left exposed the footwall of the headwall and of the sidewall faults, imparting seafloor steepening and triggering the failures that form the Slump Complex (Fig. 21d). Seepage of fluids can lead to weakening and failure of sediments (Locat and Lee, 2002). Gee et al. (2006) reported that upward migration and release of fluids along fault planes can occur during fault slip and promote slope collapse in overlaying strata. This mechanism may be particularly relevant for the initiation of the Slump Complex as the sidewall and headwall faults of the underlying megaslides may have formed important conduits for upward migration of fluids sourced from the overpressured Turonian shale detachment. This, in turn, may have promoted weakening and collapse of the upper section of the megaslides.

Earthquake shaking, due to fault rupture, generates accelerations of the sediment column that can induce shear stresses large enough to trigger the collapse of a previously stable slope (Hampton et al., 1996; Lee et al., 2007; Locat and Lee, 2002). Earthquake related stresses can also cause transient excess pore pressure leading to a degradation of shear strength and collapse of the sediment column (Lee et al., 2007). Although earthquakes are considered effective triggers of submarine landslides (e.g. Lee et al., 2007), it is suggested that this mechanism can be discarded when related to activity of megaslide faults. The reason is that these faults are not basement-involved structures, and they affect sections of sediments only few kilometres thick which are arguably poorly consolidated. These characteristics make megaslides faults likely to be aseismic (Scholz, 2002). This seems to be corroborated by the marked paucity of recent earthquakes

along margins where gravity-driven linked systems are active at the present day, such as the Niger Delta (Adewole and Healy, 2013).
The bathymetry imparted by megaslide structuring not only provided a triggering factor, it also largely impacted the emplacement of the overlying failures. This is suggested by the fact that structural highs such as lateral ramp anticlines acted as barriers, preventing further advance of the slumping masses causing their progressive thinning and termination (Fig. 21d). That similarly applies to megaslide headwall structures such as the rollover anticlines that acted as a barrier above which slumps markedly thin, but also provided weak zones prone to collapse (Fig. 21d). This highlights the control of the megaslide structures on the overall shape, extension, thickness and volume of the overlying failures.

9.2.2 Comparison with other Degradation Complexes and Wider Implications

Degradation complexes with similar seismic characteristics to those presented have been observed at the contractional toes of a number of gravity-driven linked systems such as those in the Amazonas Fan (Reis et al., 2010) and in the Niger Delta (Heini and Davies, 2006). As an example Reis et al. (2010) have reported the downslope collapse of a series of contorted, slump-like failures that deeply degraded the shallow, frontal part of the contractional domain of the Amazons gravity-driven linked system. The failures formed deposits up to 600 m thick and left behind large headscaps perched on the seaward-facing flanks of the thrust-related folds.
According to the classification of submarine landslides of Moscardelli and Wood (2008), the degradation complexes observed in Amazonas Fan and those mapped offshore Namibia, can be regarded as 'detached' failures. This is because the emplacement of these complexes is strictly controlled by local bathymetric features–the underlying megaslides structures–and are hence 'detached' from sediment sourcing regions at the edges of the margins (Moscardelli and Wood 2008). The authors of the classification suggest that because detached systems are triggered by local instabilities they are invariably of modest dimensions, with volumes in the order of few cubic kilometres. In contrast, this study indicates that detached systems such as the Namibian Slump Complex can attain to a much larger volume of material as they are linked to megaslide structures that extends for tens of kilometres. This is highlighted by the fact that the Namibian Slump Complex has an estimated volume in excess of 600 km3, a size that approaches some of the largest slope failures so far reported in the literature, such as the Sharan Debris Flow (Gee et al., 1999) and the Brunei Slide (Gee et al., 2007), both with volumes in the order of 1000 km3. For this reason, it is proposed that the failures associated with the proximal part of megaslides presented in this research, together with those occurring in their contractional toes, form a new member of detached failures termed 'megaslide-degradation complexes'.

10 Conclusions

The 3D seismic geomorphology of Late Cretaceous Namibian megaslides offers previously unattainable insight into the 4D evolution of gravity-driven linked systems. The main conclusions of this research are:

- Gravity-driven linked systems are laterally segmented into series of spoon-shaped km-wide megaslides.
- The megaslides are characterised by a headwall fault system from where material is translated downslope. Translation is accommodated laterally by a pair of sidewall fault systems.
- Extensional displacement in the proximal part of the sidewall faults form prominent sidewall horsts up to 6 km wide that laterally bound the megaslides.
- During emplacement, rotation of strata into the headwall faults as well as into the sidewall faults creates headwall rollover anticlines tens of kilometres wide.
- Downdip lateral spreading of the sliding mass induces reverse displacement in the distal segment of the sidewall systems with the formation of lateral ramps and associated anticlines up to 2 km across that laterally bound the downslope part of the megaslides.
- Lateral thrust anticline, sidewall horsts and rollover anticlines represent novel structural traps that make megaslides an attractive element of deep-water exploration along the Namibian margin and other gravitationally unstable margins.
- Structuring of the megaslides occurs through episodic, basinward stepping, sliding events separated by periods of quiescence of few millions of years. Distinct episodes of emplacement may be related to phases of enhanced sediment delivery or pulses in generation and dissipation of overpressure at the basal detachment. The lateral variations of the same mechanisms likely control the size and distribution of the megaslides.
- The activation of the headwall and sidewall systems during the structuring of the megaslides creates gravitationally unstable areas that typically collapse resulting in slump complexes with volumes of hundreds of cubic kilometres that degrade the upper inner part of the megaslides.
- Together with the classic toe degradation complexes observed at the leading edge of gravity-driven linked systems, these collapses at the headwalls and sidewalls of megaslides form a new category of 'detached failures' (sensu (Moscardelli and Wood, 2008), termed megaslide-degradation complexes, which can attain volumes of hundreds of cubic kilometres.
- The emplacement of the degradation complexes strongly reflects the distribution and nature of the underlying megaslide structures as these structures ultimately control the overall extent, thickness and size of the overlying collapse failures.

Acknowledgements
The authors grateful acknowledge Namcor and Dr. Uaapi Utjavari for providing the seismic datasets analysed in this study. The authors are deeply indebted Dr. Robert Hooper, Dr. Jose De Vera, Prof. Jake Hossack and Prof. Peter Burgess for their invaluable advice and thoughts regarding this research. A special thanks to the late Prof. David Roberts who provided feedback and encouragement during the early stages of composition of this manuscript. Resources and equipment for this research were kindly provided by the STAR Research Consortium and the Fault Dynamics Research Group. Halliburton and Russell Holroyd are thanked for kindly providing Landmark seismic interpretation software as a University Research Grant. dGB are thanked for the use of OpendTect. The authors are also indebted to Dr. Tiago Alves (3D Seismic Lab, Cardiff University) and an anonymous reviewer for their suggestions and comments.

Figure 1: Location map of the study area. a) Digital elevation model showing the location of the Orange Basin along the passive margin of Namibia. b) 3D view of the Orange Basin showing the location of the 3D seismic dataset analysed in this research. The 3D survey is located above the present-day slope of the margin. Note also the location of key seismic lines shown in Figure 2 and 4. Topography from USGS (2006), bathymetry from Amante and Eakins (2009).

Figure 2: 2D regional seismic profile crossing the Orange Basin from the outer shelf to the slope illustrating the main sequences and regional reflectors. Note the gravity-driven linked system affecting the Upper Cretaceous Sequence 3. Note also the seaward dipping reflectors within the syn-rift Upper Jurassic-Lower Cretaceous Sequence I. The marginal rift basins are not imaged in this line as they are located further to the east, beneath the innermost part of the shelf. Section location shown in Figure 1. Modified from de Vera et al. (2010).

Figure 3: Chronostratigraphic chart of the Orange Basin compiled from Gerrard and Smith (1982); Light et al. (1993); Séranne and Anka (2005). The gravity-driven features analysed in this paper are located in the Upper Cretaceous Sequence III. The Turonian open marine shales are thought to have acted as a regional detachment surface for the Late Cretaceous megaslides.

Figure 4: a) Uninterpreted and b) interpreted representative dip section through the 3D seismic volume. The section shows the lower Megaslide Complex and the overlying Slump Complex. Note the erosionally truncated upper part of the Megaslide Complex and the chaotic seismic facies of the overlying Slump Complex. Section location shown in Figures 1 & 5.

Figure 5: a) Coherency and b) shaded relief depth slices within the Megaslide Complex at depth of -3450 m. (c) Interpreted structural map. Note in panel "a" the occurrence of prominent E-W-trending sidewall faults that segment the complex into distinct megaslides. Panel "b" clearly shows that the thrust-related folds are cut and displaced by the sidewall faults. Depth-slice location shown in Figure 4.

Figure 6: 3D model showing the architecture of the central megaslide s6. Note the spoon-shaped arrangement of the headwall faults that link laterally with the sidewall faults. The model shows horizon K1 at the headwall of the megaslide, whereas horizon P1 is shown at the toe. The stratigraphic location of these surfaces is shown in Figure 4.

Figure 7: a) Uninterpreted and b) interpreted section showing the details of headwall fault system of megaslide s6. Note the listric nature of the extensional faults that delineate a series of well imaged rotated fault blocks. Growth strata associated with the extensional faults are observed above horizon K1. Note that these are truncated by the basal shear surface of the overlying Slump Complex. Section location is shown in Figure 4.

Figure 8: Seismic block diagram showing the structural architecture of the headwall of megaslide s6. The seismic blocks are cropped at horizon K1 and show the scoop-shaped morphology of the headwall of the megaslide. As the headwall faults curve and link laterally with the sidewall faults the headwall strata form a prominent 3D rollover anticline. Also note the pervasive faulting affecting the crest of the anticline.

Figure 9: Interpreted and uninterpreted strike sections showing the along-strike variation in the structural style of the sidewall faults that bound megaslides s5, s6 & s7. Note in the headwall section “a” the occurrence of growth strata above horizon K1 that thicken against the sidewall faults bounding megaslides s6 and S7. Section “c” clearly shows that horizon K1 is folded above the northern lateral ramp of megaslide s6, suggesting coeval development of this structure with the faults at the headwall of the megaslide. Also note in section “a” the pervasive faulting at the crest of the rollover anticline of megaslide 6. Sections location shown in Figure 5.

Figure 10: Seismic block diagram showing the geomorphic expression of the sidewall faults. From block “a” to block “c” the sidewall faults change from normal to reverse forming at the toe lateral ramps with associated hanging wall

anticlines. Note also the prominent sidewall horsts that divide megaslides s6 and s7. Seismic blocks cropped above horizon K0.

Figure 11: a) Uninterpreted and b) interpreted key dip section showing the details of the thrust fault system at the toe of megaslide s6. The system is formed by well imaged basinward verging, listric thrust faults with associated hanging wall anticlines. The anticlines are strongly asymmetric with steep and short forelimbs and long backlimbs. The latter comprises thick growth strata that onlap and progressively thin toward the crest of the anticlines. The Post-Kinematic unit seals and divides the syn-thrusting Syn-Kinematic I unit from the syn-extensional Syn-Kinematic II section. This indicates that the development of the headwall and sidewall systems postdates the thrust fault system. Note that the Slump Complex cut deeply into the syn-extensional Syn-Kinematic Unit II. Section location shown in Figure 4.

Figure 12: Seismic block diagram showing the along strike variation in structural style of the thrust fault system as interaction of contiguous thrust ramps occurs. Note that as fault space between faults T1 and T2 progressively decreases from block "a" to "c", T2 thrust ramp is straightened and its shape changes from sigmoidal to listric. Accordingly, the forelimb of associated F2 anticline becomes progressively shallower and parasitic folding is developed. These observations indicate that the thrust fault system developed in a forward-breaking sequence. Blocks cropped above horizon P0. Block locations shown in Figure 5.

Figure 13: a) Structural map of the basal shear surface of the Slump Complex, b) co-rendered coherency-amplitude extraction along the proportional slice within the Slump Complex. These maps were used for investigating and interpreting the internal architecture of the complex. c) Map of the interpreted structural elements of the Slump Complex showing that the complex is the result of multiple coalesced collapse features. b) Map showing the superposition of the Slump Complex on top of the Megaslide Complex. This map was used to explore the potential control of the Megaslide Complex on the architecture of the Slump Complex. See text for complete discussion.

Figure 14: a) Uninterpreted and b) interpreted detail of the co-rendered coherency-amplitude extraction along the proportional slice within the Slump Complex. The image shows the internal arrangement of slide blocks forming the norther part of the Slump Complex. See text for discussion of the interpretation. Location of the extraction is shown in Figure 13b.

Figure 15: a) Uninterpreted and b) interpreted composite section through the Slide Block N along the northern flank of the Slump Complex. The slide block is formed by a series of coherent blocks of stratigraphy evacuated by distinct headscarps. Section location shown in Figures 13 & 14. See text for discussion.

Figure 16: a) Uninterpreted and b) interpreted vertical key section through the Slump Complex showing the NW lateral termination of the complex above the underlying lateral ramp of megaslide s6. Section location shown in Figure 14.

Figure 17: a) Uninterpreted and b) interpreted detail of the co-rendered coherency and amplitude extraction along the proportional slice within the Slump Complex. The extraction shows details of the chaotic seismic facies that characterises the central part of the complex. Disrupted reflections with variable amplitude marking SE-NW-trending lineations are observed. These are interpreted as longitudinal shear surfaces that bound distinct segments of failure within the chaotic mass of the complex. Note that packages of continuos reflections are laterally constrained within the shear surfaces, these may represent slabs of relatively continuos stratigraphy transported downdip by Slump Lobe CS. Location of the extraction is shown in Figure 13b.

Figure 18: a) Uninterpreted and b) interpreted vertical key section through the Slump Complex showing dipping strata in the central part of the system. These rotated strata can be interpreted as thrust sheets or rotated blocks of stratigraphy transported within a slump. See text for explanation. Section location shown in Figure 17.

Figure 19: Exploded seismic block diagram illustrating the along strike variation in the internal structure of the Slump Complex. Block “a” shows the main headscarp and rotated blocks that form Slide Block NE. The headscarps have developed along the faults that occur at the crest of the rollover anticline of the central megaslide s6. Block “b” and “c” show that Slump Lobe SE has merged with the downdip Slump Lobe S forming a continuous contorted irregular deposit. Also note the flat relief of the basal shear of the Slump Complex above the thrust fault system of the underlying megaslide. This suggest that the these thrust faults did not control the emplacement of the Slump Complex. Blocks location shown in Figure 13c.

Figure 20: Exploded seismic block diagram illustrating the downdip variation in the internal structure of the Slump Complex. Block “a” shows Slump Lobes NE and SE that are defined by large, km-wide, basal scours. The lateral variation in thickness of these two lobes suggests that they have preferentially emplaced in structural lows at the head of the central megaslide s6. Block “b” shows the details of the rotated blocks forming Slide Block NE. Note also that the headscarps of Slide Block N have exploited the faults at the crest of the rollover anticline of megaslide s6. Location of the block is shown in Figure 13c.

Figure 21: Conceptual model showing the evolution, lateral segmentation and degradation of megaslides. The diagram is based on the results of the detailed 3D interpretation of the Orange Basin Megaslide Complex. a) Early stage of margin instability and sliding. b) Phase of quiescence and burial of early structures. c) Renewed margin instability and new episode of sliding. d) Formation of seafloor topography during megaslide emplacement that triggers megaslide-degradation complexes.

REFERENCES

Adewole, E.O., Healy, D., 2013. Quantifying in Situ Horizontal Stress in the Niger Delta Basin, Nigeria. GSTF Journal of Engineering Technology 2. doi:http://dx.doi.org/10.5176/2251-3701_2.3.88

Aldrich, J., Zilinski, R., Edman, J., Leu, W., Berge, T., Corbett, K., 2003. Documentation of a New Petroleum System in the South Atlantic. Presented at the AAPG Annual Convention, 11-14 May 2003, Salt Lake City, Utah, USA.

Alsop, G.I., Marco, S., 2014. Fold and fabric relationships in temporally and spatially evolving slump systems: A multi-cell flow model. Journal of Structural Geology 63, 27–49. doi:10.1016/j.jsg.2014.02.007

Alves, T.M., 2015. Submarine slide blocks and associated soft-sediment deformation in deep-water basins: A review. Marine and Petroleum Geology 67, 262–285. doi:10.1016/j.marpetgeo.2015.05.010

Alves, T.M., Cartwright, J.A., 2010. The effect of mass-transport deposits on the younger slope morphology, offshore Brazil. Marine and Petroleum Geology 27, 2027–2036. doi:10.1016/j.marpetgeo.2010.05.006

Austin, J.A., Uchupi, E., 1982. Continental-oceanic crustal transition off Southwest Africa. AAPG Bulletin 66, 1328–1347.

Azar, J.H., Nabi-Bidhendi, M., Javaherian, A., Pishvaie, M.R., 2009. Integrated seismic attributes to characterize a widely distributed carbonate clastic deposit system in Khuzestan Province, SW Iran. Journal of Geophysics and Engineering 6, 162.

Bahorich, M., Farmer, S., 1995. The coherence cube. The Leading Edge 14, 1053–1058.

Barnes, A.E., 2010. Shining Light on a Shady Situation. AAPG Explorer 31, 30–31.

Barnes, A.E., 2003. Shaded relief seismic attribute. Geophysics 68, 1281.

Barnes, A.E., 2002. What a Relief Shade Can Be. AAPG Explorer 8.

Bauer, K., Neben, S., Schreckenberger, B., Emmermann, R., Hinz, K., Fechner, N., Gohl, K., Schulze, A., Trumbull, R.B., Weber, K., 2000. Deep structure of the Namibia continental margin as derived from integrated geophysical studies. Journal of Geophysical Research 105, 25829–25854.

Beglinger, S.E., Doust, H., Cloetingh, S., 2012. Relating petroleum system and play development to basin evolution: West African South Atlantic basins. Marine and Petroleum Geology 30, 1–25. doi:10.1016/j.marpetgeo.2011.08.008

Ben-Avraham, Z., Hartnady, C.J.H., Kitchin, K.A., 1997. Structure and tectonics of the Agulhas-Falkland fracture zone. Tectonophysics 282, 83–98. doi:10.1016/S0040-1951(97)00213-8

Benesh, N.P., Plesch, A., Shaw, J.H., 2014. Geometry, kinematics, and displacement characteristics of tear-fault systems: An example from the deep-water Niger Delta. AAPG Bulletin 98, 465–482. doi:http://dx.doi.org/10.1306/06251311013

Bird, D., 2001. Shear margins: Continent-ocean transform and fracture zone boundaries. The Leading Edge 20, 150–159. doi:10.1190/1.1438894

Brouwer, F., 2009. Creating a good steering cube [WWW Document]. dgbes.com. URL http://dgbes.com/images/PDF/effectivedipsteeringworkflowusingbgsteering_primerodata.pdf (accessed 5.7.15).

Brown, L.F., Benson, J.M., Brink, G.J., Doherty, S., Jollands, A., Jungslager, E. H. A., Keenan, J. H. G., Muntingh, A., Van Wyk, N. J. S., 1995. Sequence Stratigraphy in Offshore South African Divergent Basins: An Atlas on Exploration for Cretaceous Lowstand Traps by Soekor (Pty) Ltd., AAPG Studies in Geology. American Association of Petroleum Geologists, Tulsa.

Bryn, P., Berg, K., Forsberg, C.F., Solheim, A., Kvalstad, T.J., 2005. Explaining the Storegga slide. Marine and Petroleum Geology 22, 11–19.

Bull, S., Cartwright, J., Huuse, M., 2009. A review of kinematic indicators from mass-transport complexes using 3D seismic data. Marine and Petroleum Geology 26, 1132–1151. doi:10.1016/j.marpetgeo.2008.09.011

Butler, R.W.H., Paton, D.A., 2010. Evaluating lateral compaction in deepwater fold and thrust belts: How much are we missing from “nature’s sandbox”? GSA Today 20, 4-10.

Butler, R.W.H., Turner, J.P., 2010. Gravitational collapse at continental margins: products and processes; an introduction. Journal of the Geological Society 167, 569–570. doi:10.1144/0016-76492010-003

Chopra, S., Marfurt, K.J., 2008. Introduction to this special section--Seismic Attributes. The Leading Edge 27, 296–297. doi:10.1190/1.2896619

Chopra, S., Marfurt, K.J., 2007. Seismic attributes for prospect identification and reservoir characterization, Seg Geophysical Developments. Society of Exploration Geophysicists, Tulsa.

Cobbold, P.R., Clarke, B.J., Loseth, H., 2009. Structural consequences of fluid overpressure and seepage forces in the outer thrust belt of the Niger Delta. Petroleum Geoscience 15, 3.

Cobbold, P.R., Mourgues, R., Boyd, K., 2004. Mechanism of thin-skinned detachment in the Amazon Fan: assessing the importance of fluid overpressure and hydrocarbon generation. Marine and Petroleum Geology 21, 1013–1025. doi:10.1016/j.marpetgeo.2004.05.003

Corredor, F., Shaw, J.H., Bilotti, F., 2005. Structural styles in the deep-water fold and thrust belts of the Niger Delta. AAPG Bulletin 89, 753–780. doi:10.1306/02170504074

Coward, M.P., Purdy, E.G., Ries, A.C., Smith, D.G., 1999. The distribution of petroleum reserves in basins of the South Atlantic margins, in: Cameron, N.R., Bate, R.H., Clure, V.S. (Eds.), The Oil and Gas Habitats of the South Atlantic, Geological Society London, Special Publications, 153. pp. 101–131.

Damuth, J.E., 1994. Neogene gravity tectonics and depositional processes on the deep Niger Delta continental margin. Marine and Petroleum Geology 11, 320, IN1–IN10, 321–346. doi:10.1016/0264-8172(94)90053-1

Dauteuil, O., Rouby, D., Braun, J., Guillocheau, F., Deschamps, F., 2013. Post-breakup evolution of the Namibian margin: Constraints from numerical modeling. Tectonophysics, Progress in understanding the South Atlantic margins 604, 122–138. doi:10.1016/j.tecto.2013.03.034

De Groot, P., Bril, B., 2005. The open source model in geosciences and OpendTect in particular. Presented at the SEG Annual Meeting, 6-11 November 2005, Houston, Texas, USA.

De Groot, P., Ligtenberg, H., Oldenziel, T., Connolly, D., Meldahl, P., 2004. Examples of Multi-attribute, Neural Network-Based Seismic Object Detection, in: Davies, R.J., Cartwright, J.A., Stewart, S.A., Lappin, M. (Eds.), Geological Society, London, Memoirs, 29. pp. 335–338.

De Vera, J., Granado, P., McClay, K., 2010. Structural evolution of the Orange Basin gravity-driven system, offshore Namibia. Marine and Petroleum Geology 27, 223–237. doi:10.1016/j.marpetgeo.2009.02.003

Dingle, R.V., 1980. Large allochthonous sediment masses and their role in the construction of the continental slope and rise off southwestern Africa. Marine Geology 37, 333–354. doi:10.1016/0025-3227(80)90109-7

Doucouré, C.M., de Wit, M.J., 2003. Old inherited origin for the present near-bimodal topography of Africa. Journal of African Earth Sciences 36, 371–388.

Eagles, G., 2007. New angles on South Atlantic opening. Geophysical Journal International 168, 353–361.

Elliott, G.M., Berndt, C., Parson, L.M., 2009. The SW African volcanic rifted margin and the initiation of the Walvis Ridge, South Atlantic. Marine Geophysical Researches 30, 207–214. doi:10.1007/s11001-009-9077-x

Emery, K.O., Uchupi, E., Bowin, C.O., Phillips, J., Simpson, E.S.W., 1975. Continental margin off western Africa: Cape St Francis (South Africa) to Walvis Ridge (South West Africa). AAPG Bulletin 59, 3–59.

Ewart, A., Milner, S.C., Armstrong, R.A., Dungan, A.R., 1998. Etendeka Volcanism of the Goboboseb Mountains and Messum Igneous Complex, Namibia. Part I: Geochemical Evidence of Early Cretaceous Tristan Plume Melts and the Role of Crustal Contamination in the Paraná–Etendeka CFB. Journal of Petrology 39, 191 –225. doi:10.1093/petroj/39.2.191

Farrukh, Q., 2009. Apparent dip attribute in OpendTect [WWW Document]. dgbes.com. URL http://www.dgbes.com/images/PDF/howto-apparentdipattrib-steeringcube.pdf (accessed 5.7.15).

Fleming, R.W., Johnson, A.M., 1989. Structures associated with strike-slip faults that bound landslide elements. Engineering Geology 27, 39–114. doi:http://dx.doi.org/10.1016/0013-7952(89)90031-8

Frey-Martínez, J., Cartwright, J., Hall, B., 2005. 3D seismic interpretation of slump complexes: examples from the continental margin of Israel. Basin Research 17, 83–108. doi:10.1111/j.1365-2117.2005.00255.x

Gallagher, K., Brown, R., 1999a. Denudation and uplift at passive margins: the record on the Atlantic Margin of southern Africa. Philosophical Transactions of the Royal Society of London. Series A: Mathematical, Physical and Engineering Sciences 357, 835–859. doi:10.1098/rsta.1999.0354

Gallagher, K., Brown, R.W., 1999b. The Mesozoic denudation history of the Atlantic margins of southern Africa and southeast Brazil and the relationship to offshore sedimentation, in: Cameron, N.R., Bate, R.H., Clure, V.S. (Eds.), The Oil and Gas Habitats of the South Atlantic, Geological Society, London, Special Publications, 153. pp. 41–53.

Gamboa, D., Alves, T., Cartwright, J., Terrinha, P., 2010. MTD distribution on a “passive” continental margin: The Espírito Santo Basin (SE Brazil) during the Palaeogene. Marine and Petroleum Geology 27, 1311–1324. doi:10.1016/j.marpetgeo.2010.05.008

Gee, Masson, D.G., Watts, Allen, 1999. The Saharan debris flow: an insight into the mechanics of long runout submarine debris flows. Sedimentology 46, 317–335. doi:http://dx.doi.org/10.1046/j.1365-3091.1999.00215.x

Gee, M.J.R., Gawthorpe, R.L., Friedmann, S.J., 2006. Triggering and evolution of a giant submarine landslide, offshore Angola, revealed by 3D seismic stratigraphy and geomorphology. Journal of Sedimentary Research 76, 9–19.

Gee, M.J.R., Uy, H.S., Warren, J., Morley, C.K., Lambiase, J.J., 2007. The Brunei slide: A giant submarine landslide on the North West Borneo Margin revealed by 3D seismic data. Marine Geology 246, 9–23. doi:10.1016/j.margeo.2007.07.009

Gerrard, I., Smith, G.C., 1982. Post-Paleozoic succession and structure of the Southwestern African continental margin, in: Watkins, J.S., Drake, C.L. (Eds.), Studies in Continental Margin Geology: AAPG Memoir, 34. pp. 49–74.

Gladczenko, T.P., Hinz, K., Eldholm, O., Meyer, H., Neben, S., Skogseid, J., 1997. South Atlantic volcanic margins. Journal of the Geological Society 154, 465–470. doi:10.1144/gsjgs.154.3.0465

Gladczenko, T.P., Skogseid, J., Eldhom, O., 1998. Namibia volcanic margin. Marine Geophysical Researches 20, 313–341. doi:10.1023/A:1004746101320

Guillocheau, F., Rouby, D., Robin, C., Helm, C., Rolland, N., Le Carlier de Veslud, C., Braun, J., 2012. Quantification and causes of the terrigeneous sediment budget at the scale of a continental margin: a new method applied to the Namibia-South Africa margin: Quantification and causes of the terrigeneous sediment budget at the scale of a continental margin. Basin Research 24, 3–30. doi:10.1111/j.1365-2117.2011.00511.x

Hampton, M.A., Lee, H.J., Locat, J., 1996. Submarine Landslides. Reviews of Geophysics 34, 33–59.

Hawkesworth, C.J., Gallagher, K., Kelley, S., Mantovani, M., Peate, D.W., Regelous, M., Rogers, N.W., 1992. Paraná magmatism and the opening of the South Atlantic, in: Storey, B.C., Alabaster, T., Pankhurst, R.J. (Eds.), Geological Society London Special Publications, 68. pp. 221–240.

Heine, C., Zoethout, J., Müller, R.D., 2013. Kinematics of the South Atlantic rift. Solid Earth 4, 215–253. doi:10.5194/se-4-215-2013

Heini, P., Davies, R.J., 2006. Degradation of compressional fold belts: Deep-water Niger Delta. AAPG bulletin 90, 753–770.

Hesthammer, J., Fossen, H., 1999. Evolution and geometries of gravitational collapse structures with examples from the StatfJord Field, northern North Sea. Marine and Petroleum Geology 16, 259–281. doi:10.1016/S0264-8172(98)00071-3

Hirsch, K.K., Scheck-Wenderoth, M., van Wees, J.-D., Kuhlmann, G., 2010. Tectonic subsidence history and thermal evolution of the Orange Basin. Marine and Petroleum Geology 27, 565–584. doi:10.1016/j.marpetgeo.2009.06.009

Iacopini, D., Butler, R.W.., 2011. Imaging deformation in submarine thrust belts using seismic attributes. Earth and Planetary Science Letters 302, 414–422.

Jackson, C., 2012. The initiation of submarine slope failure and the emplacement of mass transport complexes in salt-related minibasins: A three-dimensional seismic-reflection case study from the Santos Basin, offshore Brazil. Geological Society of America Bulletin 124, 746–761. doi:10.1130/B30554.1

Jackson, M., Cramez, C., Fonck, J.M., 2000. Role of subaerial volcanic rocks and mantle plumes in creation of South Atlantic margins: implications for salt tectonics and source rocks. Marine and Petroleum Geology 17, 477–498.

Judd, A.G., Hovland, M., 2007. Seabed fluid flow: the impact of geology, biology and the marine environment. Cambridge University Press.

Jungslager, E.H.A., 1999. Petroleum habitats of the Atlantic margin of South Africa, in: Cameron, N.R., Bate, R.H, Clure, V.S. (Eds.), The Oil and Gas Habitats of the South Atlantic, Geological Society, London, Special Publications, 153. pp. 153–168.

Koopmann, H., Franke, D., Schreckenberger, B., Schulz, H., Hartwig, A., Stollhofen, H., di Primio, R., 2014. Segmentation and volcano-tectonic characteristics along the SW African continental margin, South Atlantic, as derived from multichannel seismic and potential field data. Marine and Petroleum Geology 50, 22–39. doi:10.1016/j.marpetgeo.2013.10.016

Kounov, A., Viola, G., de Wit, M., Andreoli, M.A.G., 2009. Denudation along the Atlantic passive margin: new insights from apatite fission-track analysis on the western coast of South Africa, in: Lisker, F., Ventura, B., Glasmacher, U. A. (Eds.), Thermochronological Methods: From Palaeotemperature Constraints to Landscape Evolution Models, Geological Society, London, Special Publications, 324. pp. 287–306.

Kuhlmann, G., Adams, S., Campher, C., van der Spuy, D., di Primio, R., Horsfield, B., 2010. Passive margin evolution and its controls on natural gas leakage in the southern Orange Basin, blocks 3/4, offshore South Africa. Marine and Petroleum Geology 27, 973–992.

Kvalstad, T.J., Andresen, L., Forsberg, C.F., Berg, K., Bryn, P., Wangen, M., 2005. The Storegga slide: evaluation of triggering sources and slide mechanics. Marine and Petroleum Geology 22, 245–256.

Law, C., 2011. Northern Mozambique: True "Wildcat" Exploration in East Africa. Presented at the AAPG Annual Convention, 10-13 April 2011, Houston, Texas, USA.

Lawrence, S.R., Munday, S., Bray, R., 2002. Regional geology and geophysics of the eastern Gulf of Guinea (Niger Delta to Rio Muni). The Leading Edge 21, 1112–1117. doi:10.1190/1.1523752

Leduc, A.M., Davies, R.J., Densmore, A.L., Imber, J., 2012. The lateral strike-slip domain in gravitational detachment delta systems: A case study of the northwestern margin of the Niger Delta. AAPG bulletin 96, 709–728.

Lee, H.J., Locat, J., Desgagnés, P., Parsons, J.D., McAdoo, B.G., Orange, D.L., Puig, P., Wong, F.L., Dartnell, P., Boulanger, E., 2007. Submarine Mass Movements on Continental Margins, in: Nittrouer, C.A., Austin, J.A., Field, M.E., Kravitz, J.H., Syvitski, J.P.M., Wiberg, P.L. (Eds.), Continental Margin Sedimentation: From Sediment Transport to Sequence Stratigraphy, Special Publication of the International Association Of Sedimentologists, 37. Wiley-Blackwell, pp. 213–274.

Light, M.P.R., Maslanyj, M.P., Greenwood, R.J., Banks, N.L., 1993. Seismic sequence stratigraphy and tectonics offshore Namibia, in: Willams, G., Dobb, A. (Eds.), Tectonic and Seismic Sequence Stratigraphy, Geological Society, London, Special Publications, 71. pp. 163–191.

Lithgow-Bertelloni, C., Silver, P.G., 1998. Dynamic topography, plate driving forces and the African superswell. Nature 395, 269–272.

Locat, J., Lee, H.J., 2002. Submarine landslides: advances and challenges. Canadian Geotechnical Journal 39, 193–212.

Macdonald, D., Gomez-Perez, I., Franzese, J., Spalletti, L., Lawver, L., Gahagan, L., Dalziel, I., Thomas, C., Trewin, N., Hole, M., Paton, D., 2003. Mesozoic break-up of SW Gondwana: implications for regional hydrocarbon potential of the southern South Atlantic. Marine and Petroleum Geology 20, 287–308. doi:10.1016/S0264-8172(03)00045-X

Marfurt, K.J., Alves, T.M., 2015. Pitfalls and limitations in seismic attribute interpretation of tectonic features. Interpretation 3, SB5–SB15. doi:10.1190/INT-2014-0122.1

Marfurt, K.J., Kirlin, R.L., Farmer, S.L., Bahorich, M.S., 1998. 3-D seismic attributes using a semblance-based coherency algorithm. Geophysics 63, 1150–1165.

McAdoo, B.G., Pratson, L.F., Orange, D.L., 2000. Submarine landslide geomorphology, US continental slope. Marine Geology 169, 103–136.

McMillan, I.K., 2003. Foraminiferally defined biostratigraphic episodes and sedimentation pattern of the Cretaceous drift succession (Eearly Barremlan to Late Maastrichtian) in seven basins

on the South African and southern Namibian continental margin. South African Journal of Science 99, 537–576.

Mello, M.R., Azambuja, N., Mohriak, W.U., Catto, A.J., Françolin, J.B., 2011. Promising giant new hydrocarbon frontier: the Namibian continental margin. GeoExpro 8, 64–69.

Middleton, G.V., 2003. Encyclopedia of sediments and sedimentary rocks. Springer.

Morley, C.K., 2009. Growth of folds in a deep-water setting. Geosphere 5, 59–89. doi:10.1130/GES00186.1

Morley, C.K., 2003. Mobile shale related deformation in large deltas developed on passive and active margins, in: van Rensbergen, P., Hills, P., Maltman, A.J., Morley, C. K. (Eds.), Subsurface Sediment Mobilization, Geological Society London, Special Publications, 216. pp. 335–358.

Morley, C.K., King, R., Hillis, R., Tingay, M., Backe, G., 2011. Deepwater fold and thrust belt classification, tectonics, structure and hydrocarbon prospectivity: A review. Earth-Science Reviews 104, 41–91. doi:10.1016/j.earscirev.2010.09.010

Moscardelli, L., Wood, L., 2008. New classification system for mass transport complexes in offshore Trinidad. Basin Research 20, 73–98.

Moscardelli, L., Wood, L., Mann, P., 2006. Mass-transport complexes and associated processes in the offshore area of Trinidad and Venezuela. AAPG Bulletin 90, 1059–1088. doi:10.1306/02210605052

Mourgues, R., Cobbold, P.R., 2006. Sandbox experiments on gravitational spreading and gliding in the presence of fluid overpressures. Journal of Structural Geology 28, 887–901.

Mourgues, R., Lecomte, E., Vendeville, B., Raillard, S., 2009. An experimental investigation of gravity-driven shale tectonics in progradational delta. Tectonophysics 474, 643–656. doi:10.1016/j.tecto.2009.05.003

O'Connor, J.M., Duncan, R.A., 1990. Evolution of the Walvis Ridge-Rio Grande Rise hot spot system: Implications for African and South American plate motions over plumes. Journal of Geophysical Research 95, 17475.

Oliveira, M.J.R.., Santarem, P., Moraes, A., Zalán, P.V., Caldeira, J.L., Tanaka, A., Trosdtorf Jr., I., 2013. Linked Extensional-compressional Tectonics in Gravitational Systems in the Equatorial Margin of Brazil, in: Gao, D. (Ed.), Tectonics and Sedimentation. American Association of Petroleum Geologists, Tulsa, Oklahoma, pp. 159–178.

Parise, M., 2003. Observation of surface features on an active landslide, and implications for understanding its history of movement. Natural Hazards and Earth System Science 3, 569–580. doi:http://dx.doi.org/10.5194/nhess-3-569-2003

Paton, D.A., van der Spuy, D., di Primio, R., Horsfield, B., 2008. Tectonically induced adjustment of passive-margin accommodation space; influence on the hydrocarbon potential of the Orange Basin, South Africa. AAPG Bulletin 92, 589.

Peate, D.W., Hawkesworth, C.J., Mantovani, M.S.., Shukowsky, W., 1990. Mantle plumes and flood-basalt stratigraphy in the Paraná, South America. Geology 18, 1223.

Peel, F.J., 2014. The engines of gravity-driven movement on passive margins: Quantifying the relative contribution of spreading vs. gravity sliding mechanisms. Tectonophysics 633, 126–142. doi:10.1016/j.tecto.2014.06.023

Peel, F.J., Travis, C.J., Hossack, J.R., 1995. Genetic structural provinces and salt tectonics of the Cenozoic offshore US Gulf of Mexico: A preliminary analysis, in: Jackson, M.P.A., Roberts, D.G., Snelson, S. (Eds.), Salt Tectonics: A Global Perspective, AAPG Memoirs, 65. pp. 153–176.

Pickering, K.T., Hiscott, R.N., 2015. Deep-marine systems: processes, deposits, environments, tectonics and sedimentation. John Wiley & Sons Inc, Chichester, West Sussex ; Hoboken, NJ.

Posamentier, H.W., Davies, R.J., Cartwright, J.A., Wood, L., 2007. Seismic geomorphology - an overview, in: Davies, R. J., Posamentier, H. W., Wood, L. J. (Eds.), Seismic Geomorphology: Applications to Hydrocarbon Exploration and Production, Geological Society, London, Special Publications, 227. pp. 1–14.

Posamentier, H.W., Martinsen, O.J., 2011. The character and genesis of submarine mass-transport deposits: insights from outcrop and 3d seismic data, in: Shipp, R.C., Posamentier, H.W. (Eds.), Mass-Transport Deposits in Deepwater Settings, SEPM Special Publication, 96. pp. 7–38.

Prior, D.B., Bornhold, B.D., Johns, M.W., 1984. Depositional characteristics of a submarine debris flow. The Journal of Geology 92, 707–727.

Raab, M.J., Brown, R.W., Gallagher, K., Carter, A., Weber, K., 2002. Late Cretaceous reactivation of major crustal shear zones in northern Namibia: constraints from apatite fission track analysis. Tectonophysics 349, 75–92.

Raab, M.J., Brown, R.W., Gallagher, K., Weber, K., Gleadow, A.J.W., 2005. Denudational and thermal history of the Early Cretaceous Brandberg and Okenyenya igneous complexes on Namibia's Atlantic passive margin. Tectonics 24, 1–15. doi:10.1029/2004TC001688

Reis, A.T., Perovano, R., Silva, C.G., Vendeville, B.C., Araujo, E., Gorini, C., Oliveira, V., 2010. Two-scale gravitational collapse in the Amazon Fan: a coupled system of gravity tectonics and mass-transport processes. Journal of the Geological Society 167, 593–604. doi:10.1144/0016-76492009-035

Richardson, S.E., Davies, R.J., Allen, M.B., Grant, S.F., 2011. Structure and evolution of mass transport deposits in the South Caspian Basin, Azerbaijan. Basin Research 23, 702–719. doi:10.1111/j.1365-2117.2011.00508.x

Rowan, M.G., Peel, F.J., Vendeville, B.C., 2004. Gravity-driven fold belts on passive margins, in: McClay, K.R. (Ed.), Thrust Tectonics and Hydrocarbon Systems, AAPG Memoirs, 82. pp. 157–182.

Roy, C.L., Rangin, C., Pichon, X.L., Ngoc, H.N.T., Andreani, L., Aranda-Garcia, M., 2008. Neogene crustal shear zone along the western Gulf of Mexico margin and its implications

for gravity sliding processes. Evidences from 2D and 3D multichannel seismic data. Bulletin de la Societe Geologique de France 179, 175–193. doi:10.2113/gssgfbull.179.2.175

Rust, D.J., Summerfield, M.A., 1990. Isopach and borehole data as indicators of rifted margin evolution in southwestern Africa. Marine and Petroleum Geology 7, 277–287. doi:10.1016/0264-8172(90)90005-2

Sawyer, D.E., Flemings, P.B., Dugan, B., Germaine, J.T., 2009. Retrogressive failures recorded in mass transport deposits in the Ursa Basin, Northern Gulf of Mexico. Journal of Geophysical Research 114, B10102. doi:10.1029/2008JB006159.

Scarselli, N., 2014. Seismic Analysis of Gravity-Driven Deformation at Passive Margins. Unpublished Ph.D. thesis, Royal Holloway, University of London.

Scarselli, N., McClay, K., Elders, C., 2013. Submarine slide and slump complexes, Exmouth Plateau, NW Shelf of Australia, in: Keep, M., Moss, S.J. (Eds.), The Sedimentary Basins of Western Australia IV: Proceedings of the Petroleum Exploration Society of Australia Symposium. Perth, WA.

Scholz, C.H., 2002. The Mechanics of Earthquakes and Faulting, 2nd ed. Cambridge University Press, Cambridge.

Schultz-Ela, D.D., 2001. Excursus on gravity gliding and gravity spreading. Journal of Structural Geology 23, 725–731. doi:10.1016/S0191-8141(01)00004-9

Séranne, M., Anka, Z., 2005. South Atlantic continental margins of Africa: A comparison of the tectonic vs climate interplay on the evolution of equatorial west Africa and SW Africa margins. Journal of African Earth Sciences 43, 283–300. doi:10.1016/j.jafrearsci.2005.07.010

Soares, D.M., Alves, T.M., Terrinha, P., 2014. Contourite drifts on early passive margins as an indicator of established lithospheric breakup. Earth and Planetary Science Letters 401, 116–131. doi:10.1016/j.epsl.2014.06.001

Soares, D.M., Alves, T.M., Terrinha, P., 2012. The breakup sequence and associated lithospheric breakup surface: Their significance in the context of rifted continental margins (West Iberia and Newfoundland margins, North Atlantic). Earth and Planetary Science Letters 355-356, 311–326. doi:10.1016/j.epsl.2012.08.036

Stewart, S.A., 1999. Geometry of thin-skinned tectonic systems in relation to detachment layer thickness in sedimentary basins. Tectonics 18, 719–732.

Summerhayes, C.P., Bornhold, B.D., Embley, R.W., 1979. Surficial slides and slumps on the continental slope and rise of South West Africa: A reconnaissance study. Marine Geology 31, 265–277. doi:10.1016/0025-3227(79)90037-9

Tinker, J., de Wit, M., Brown, R., 2008. Mesozoic exhumation of the southern Cape, South Africa, quantified using apatite fission track thermochronology. Tectonophysics 455, 77–93.

Torsvik, T.H., Rousse, S., Labails, C., Smethurst, M.A., 2009. A new scheme for the opening of the South Atlantic Ocean and the dissection of an Aptian salt basin. Geophysical Journal International 177, 1315–1333.

Trincardi, F., Argnani, A., 1990. Gela submarine slide: A major basin-wide event in the plio-quaternary foredeep of Sicily. Geo-Marine Letters 10, 13–21. doi:10.1007/BF02431017

Turner, J.P., 1995. Gravity-driven structures and rift basin evolution; Rio Muni Basin, offshore equatorial West Africa. AAPG Bulletin 79, 1138–1158.

Vendeville, B.C., 2005. Salt tectonics driven by sediment progradation: Part I--Mechanics and kinematics. AAPG Bulletin 89, 1071–1079. doi:10.1306/03310503063

Welbon, A.I.F., Brockbank, P.J., Brunsden, D., Olsen, T.S., 2007. Characterizing and producing from reservoirs in landslides: challenges and opportunities, in: Barr, D., Walsh, J.J., Knipe R.J. (Eds.), Structurally Complex Reservoirs, Geological Society London, Special Publications, 292. pp. 49–74.

Wickens, H., McLachlan, I.R., 1990. The stratigraphy and sedimentology of the reservoir interval of the Kudu 9A-2 and 9A-3 boreholes. Communications of the Geological Society of Namibia 6, 9–22.

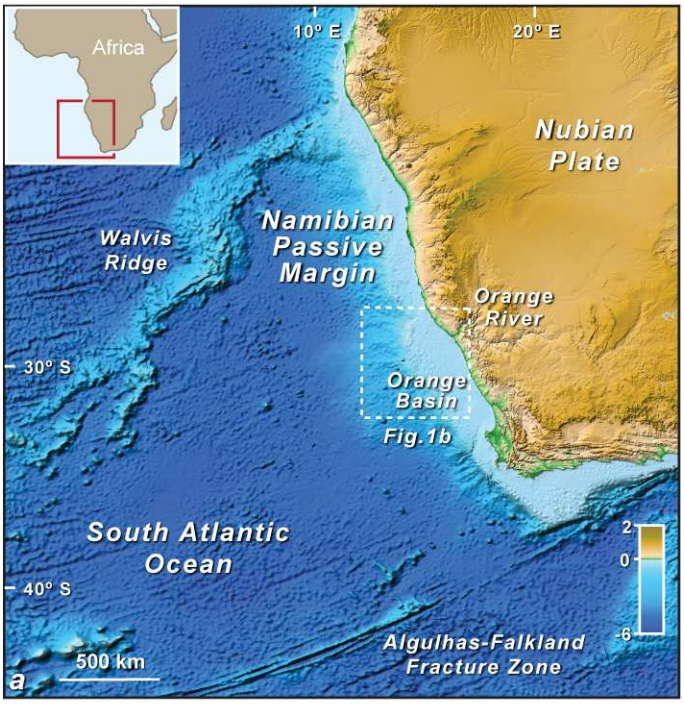

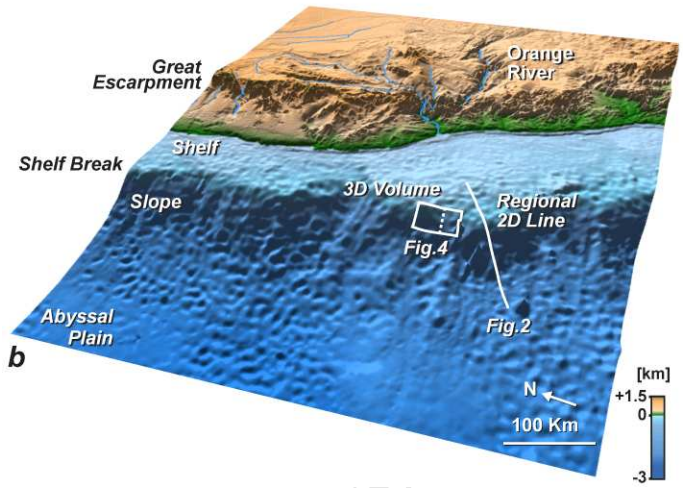

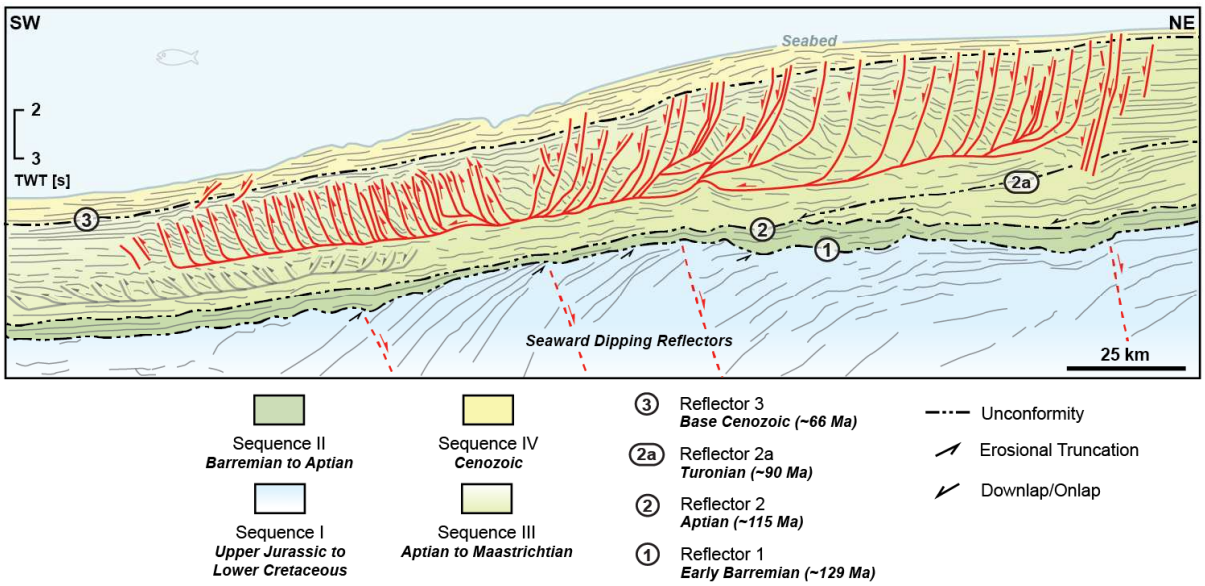

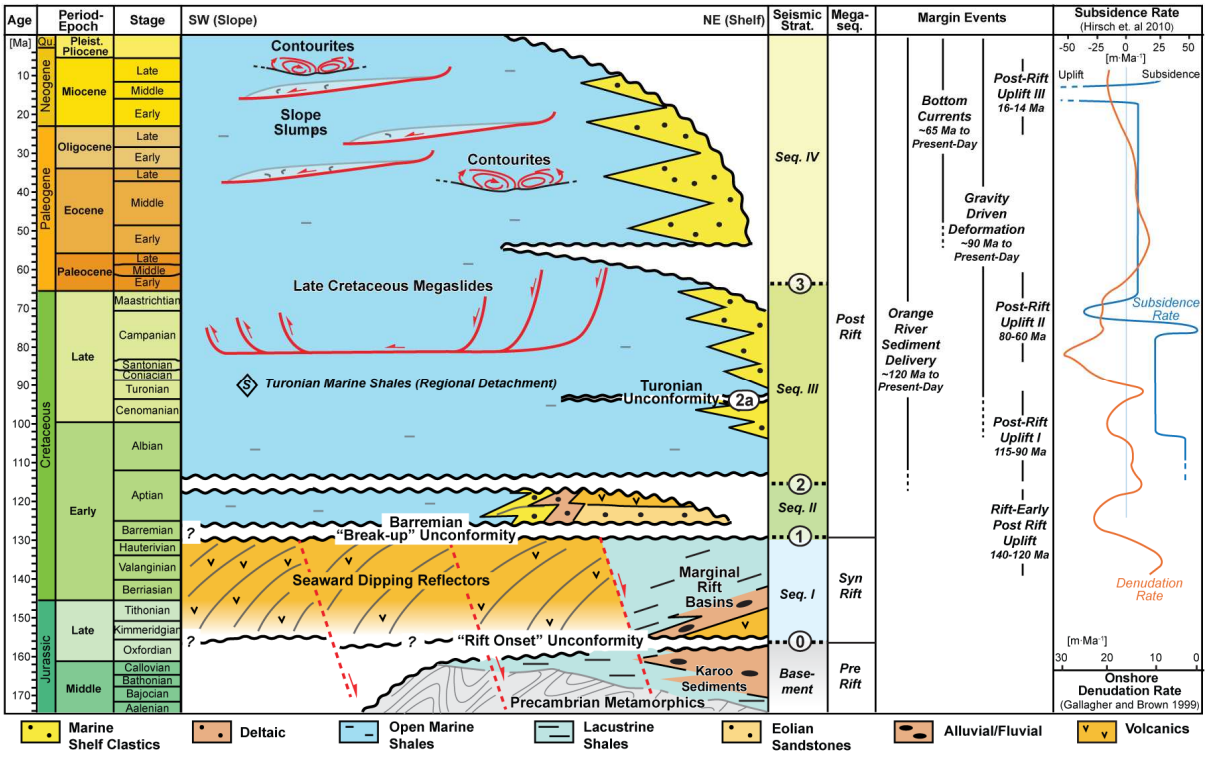

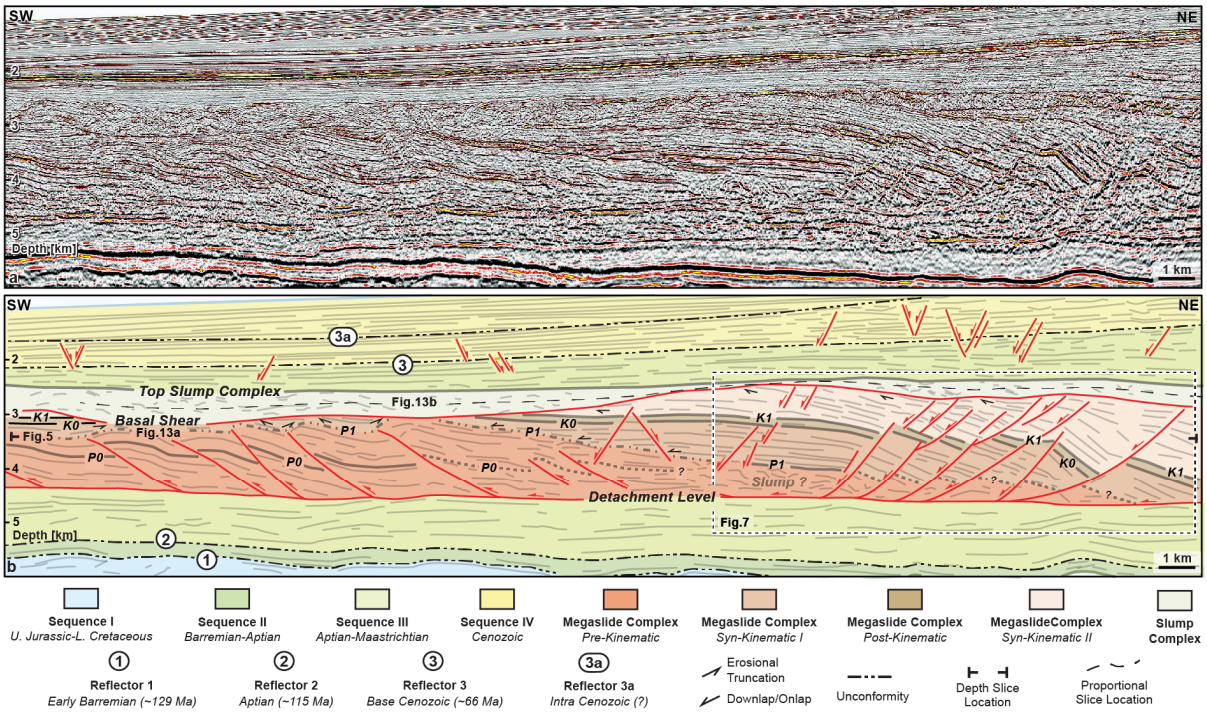

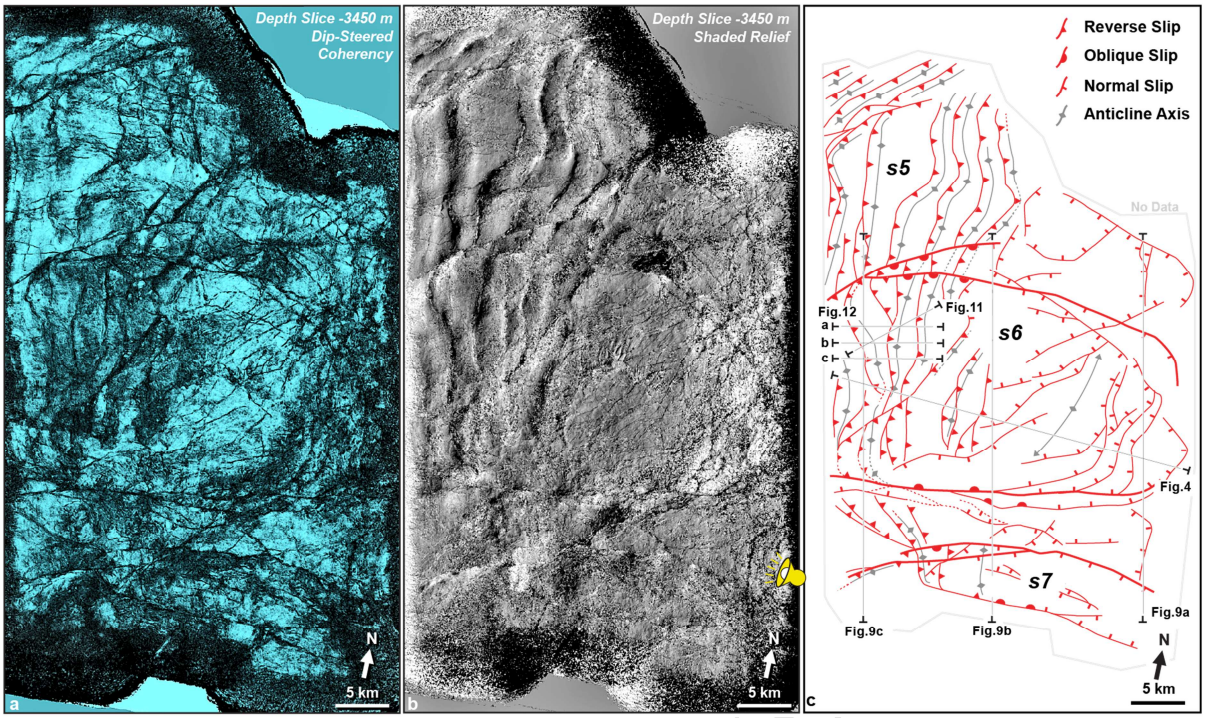

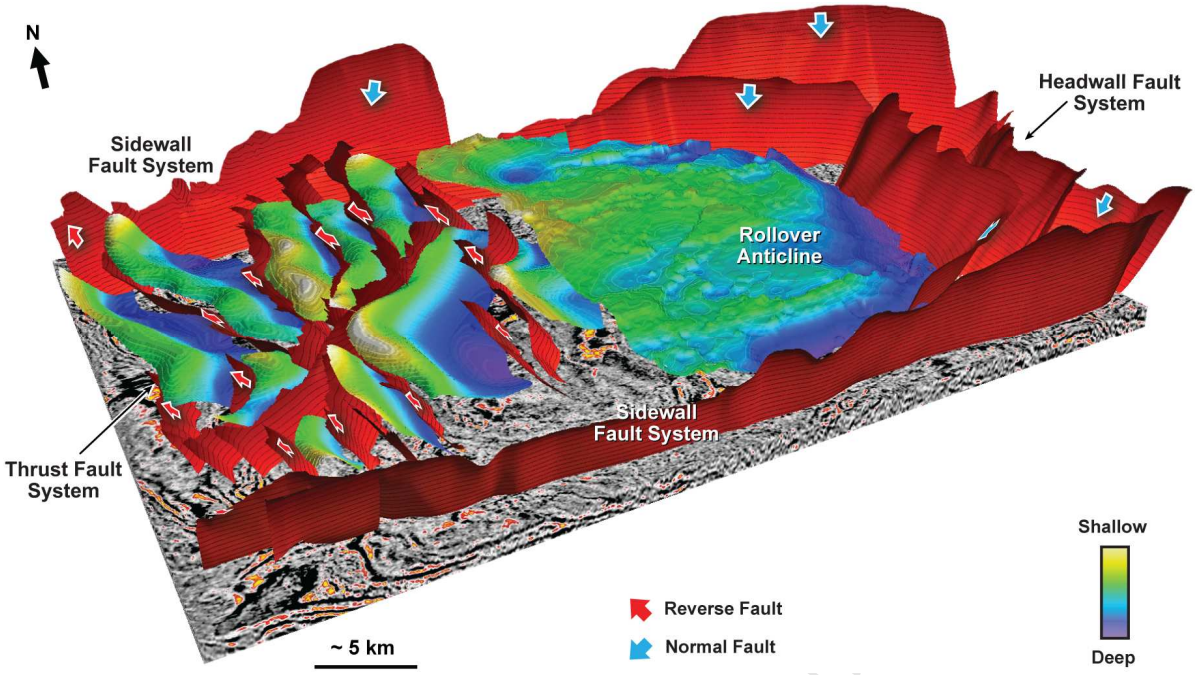

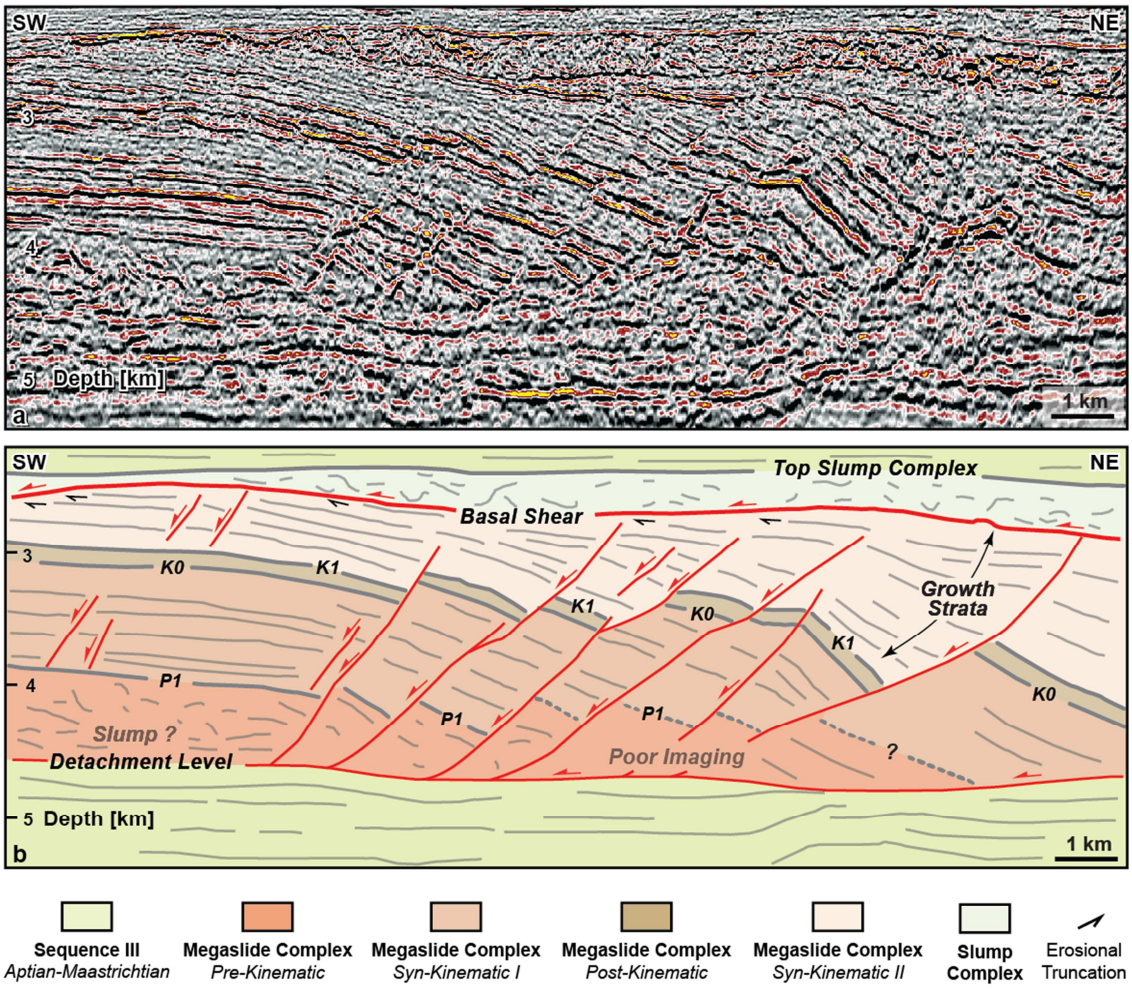
SW
NE
3
4
5 Depth [km]
a
1 km
SW
NE
Top Slump Complex
Basal Shear
3
K0
K1
K1
K0
K1
Growth
Strata
4
P1
P1
P1
K0
Slump ?
Detachment Level
Poor Imaging
?
5 Depth [km]
b
1 km
Sequence III
Aptian-Maastrichtian
Megaslide Complex
Pre-Kinematic
Megaslide Complex
Syn-Kinematic I
Megaslide Complex
Post-Kinematic
Megaslide Complex
Syn-Kinematic II
Slump
Complex
Erosional
Truncation

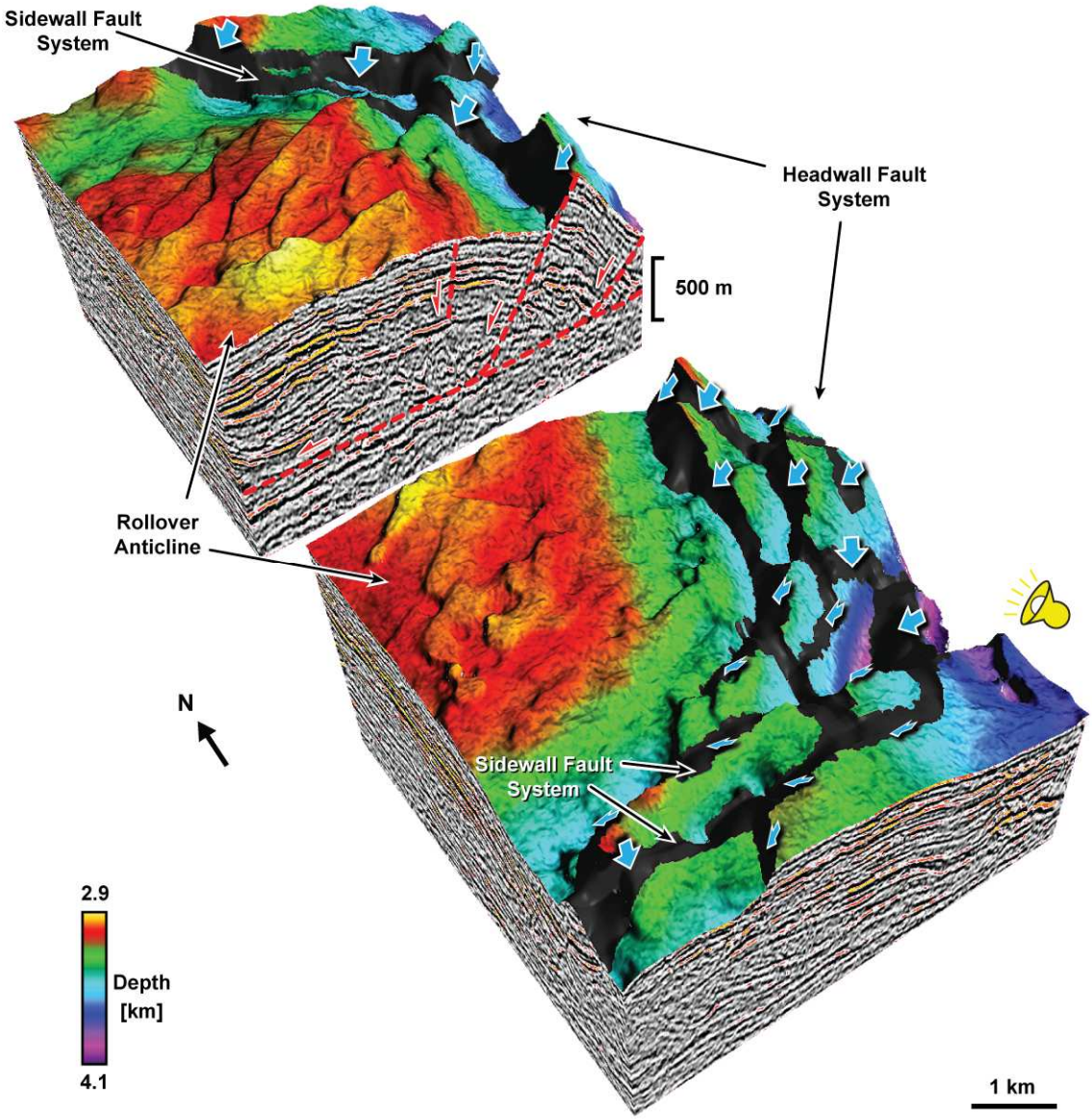
Sidewall Fault System
Headwall Fault System
500 m
Rollover Anticline
N
Sidewall Fault System
2.9
Depth [km]
4.1
1 km

a) Headwall Strike Line

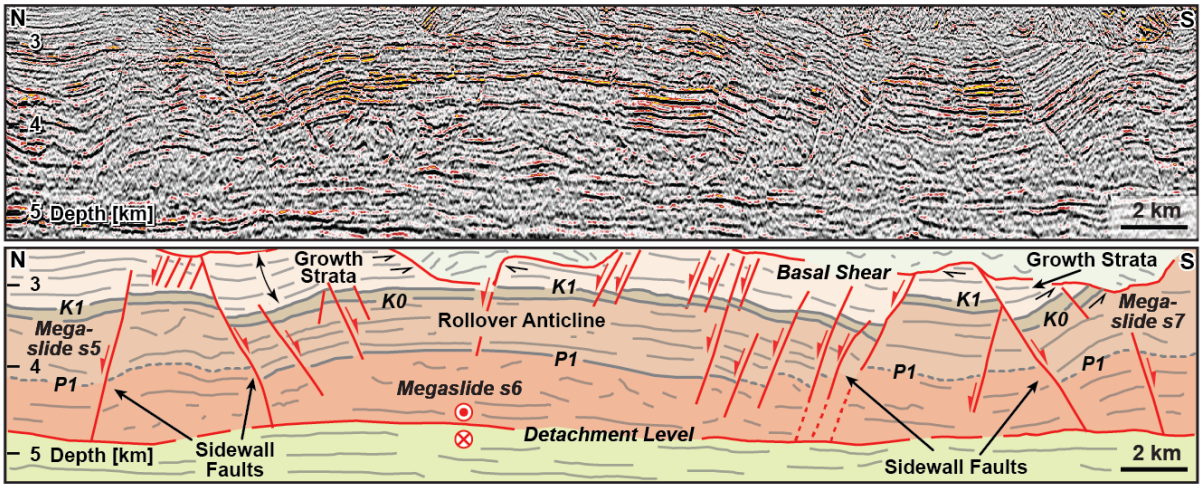

b) Mid Strike Line

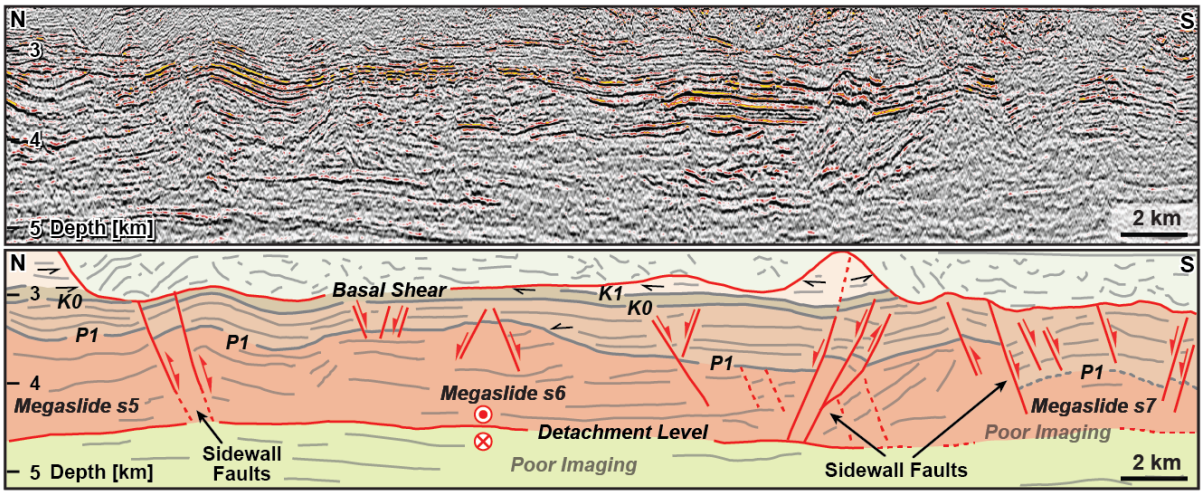

c) Toe Strike Line

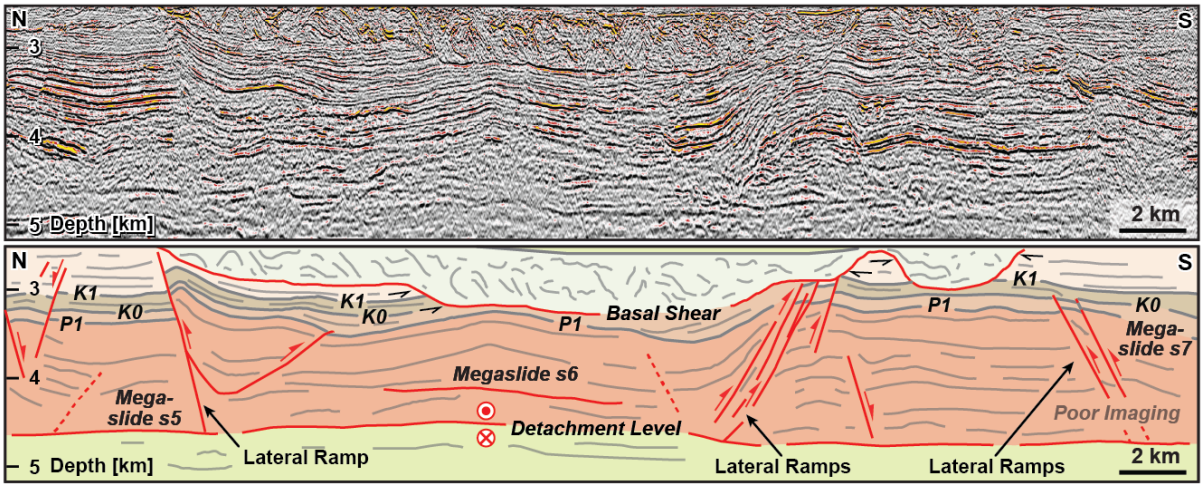

Sequence III
Aptian-Maastrichtian

Megaslide Complex
Pre-Kinematic

Megaslide Complex
Syn-Kinematic I

Megaslide Complex
Post-Kinematic

Megaslide Complex
Syn-Kinematic II

Slump Complex

Erosional Truncation

Downlap/ Onlap

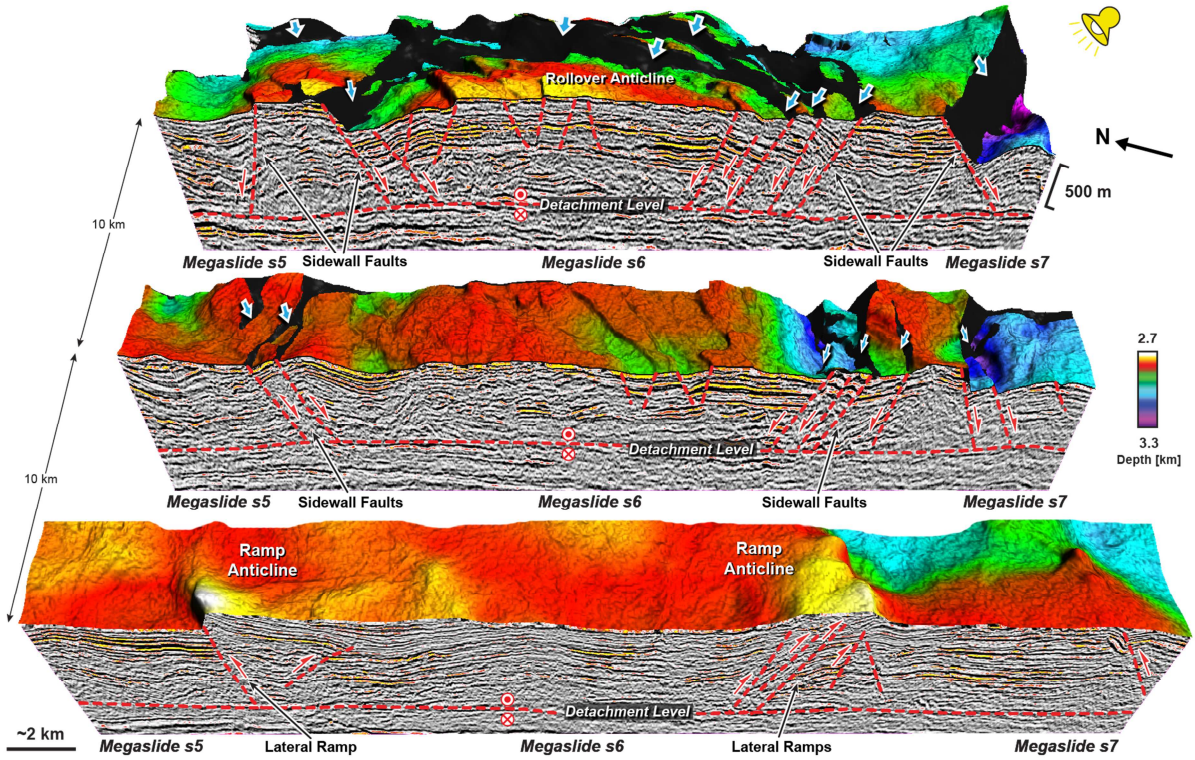

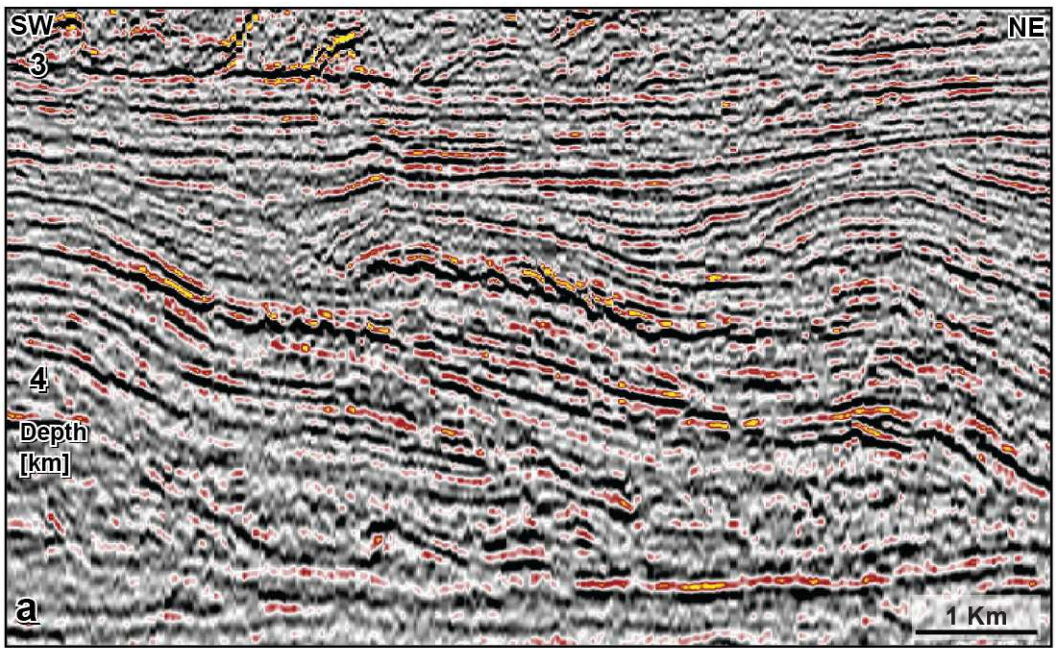
SW
NE
3
4
Depth
[km]
a
1 Km

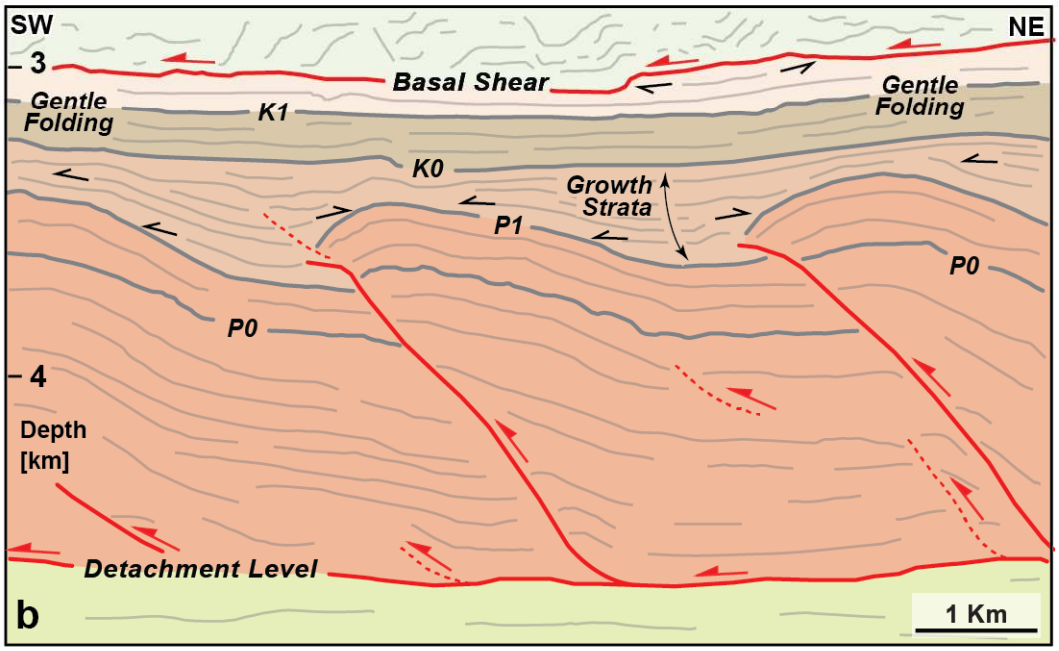
SW
NE
3
Basal Shear
Gentle
Folding
K1
Gentle
Folding
K0
Growth
Strata
P1
P0
P0
4
Depth
[km]
Detachment Level
b
1 Km

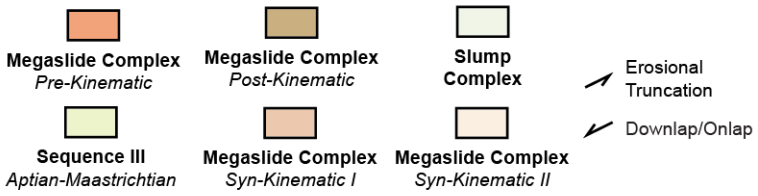
Megaslide Complex
Pre-Kinematic
Megaslide Complex
Post-Kinematic
Slump
Complex
Erosional
Truncation
Sequence III
Aptian-Maastrichtian
Megaslide Complex
Syn-Kinematic I
Megaslide Complex
Syn-Kinematic II
Downlap/Onlap

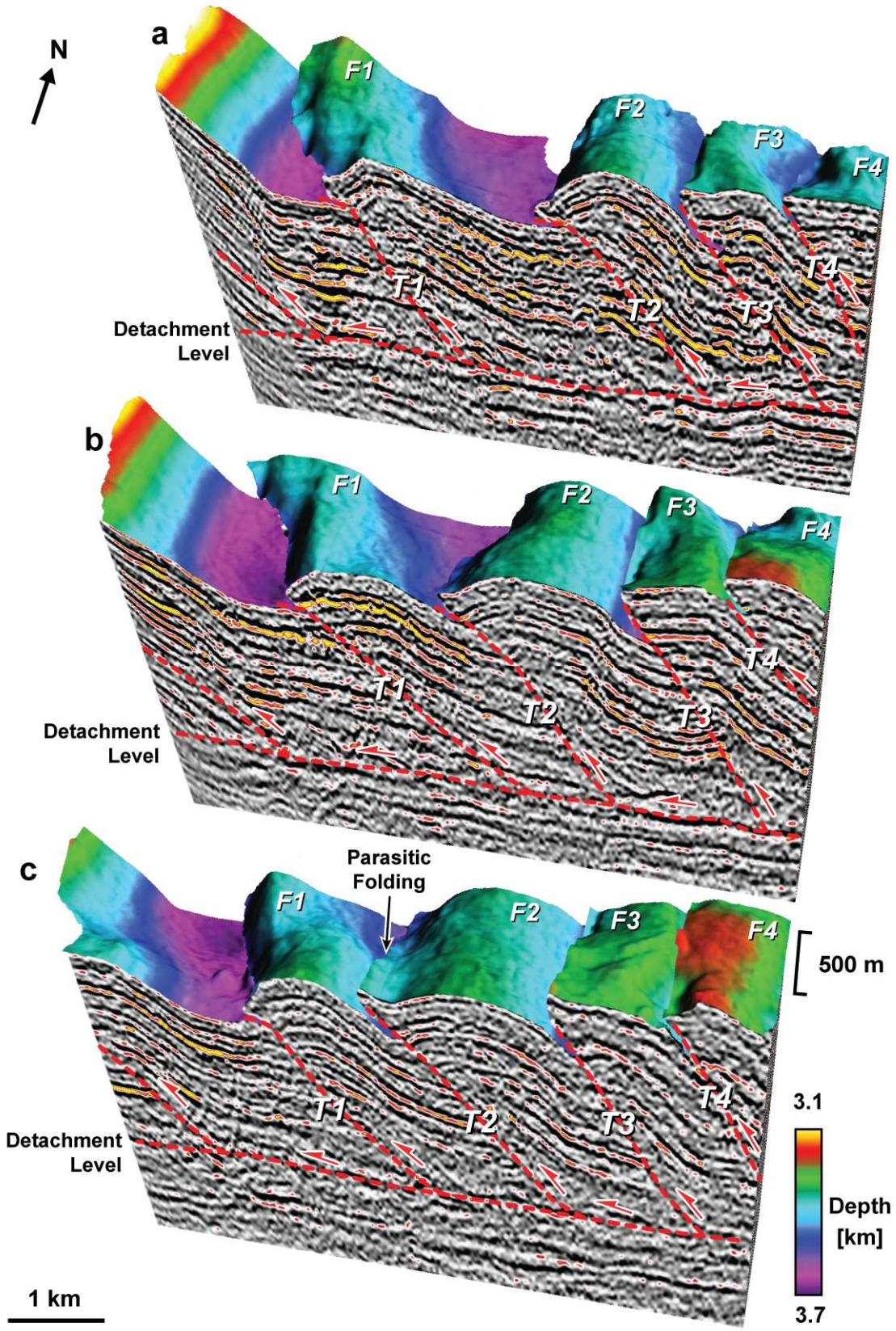
N
a
F1
F2
F3
F4
T1
T2
T3
T4
Detachment Level
b
F1
F2
F3
F4
T1
T2
T3
T4
Detachment Level
c
Parasitic Folding
F1
F2
F3
F4
T1
T2
T3
T4
Detachment Level
500 m
3.1
Depth [km]
3.7
1 km

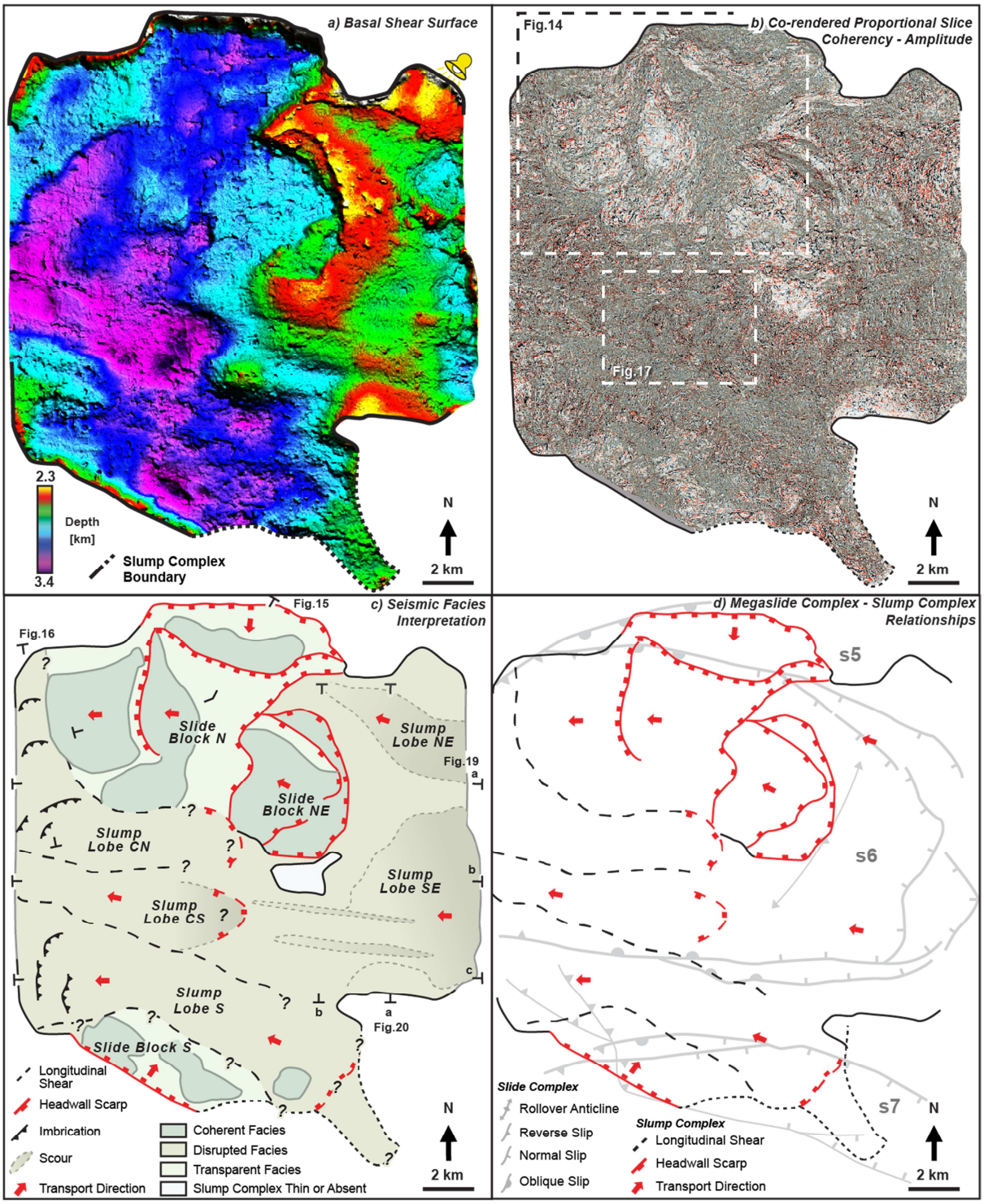
a) Basal Shear Surface
2.3
Depth
[km]
3.4
Slump Complex
Boundary
N
2 km
Fig.14
b) Co-rendered Proportional Slice
Coherency - Amplitude
Fig.17
N
2 km
Fig.15
Fig.16
c) Seismic Facies
Interpretation
Slide
Block N
Slump
Lobe NE
Fig.19
a
Slide
Block NE
Slump
Lobe CN
Slump
Lobe SE
b
Slump
Lobe CS
c
Slump
Lobe S
a
b
Fig.20
Slide Block S
Longitudinal
Shear
Headwall Scarp
Imbrication
Scour
Transport Direction
Coherent Facies
Disrupted Facies
Transparent Facies
Slump Complex Thin or Absent
N
2 km
d) Megaslide Complex - Slump Complex
Relationships
s5
s6
s7
Slide Complex
Rollover Anticline
Reverse Slip
Normal Slip
Oblique Slip
Slump Complex
Longitudinal Shear
Headwall Scarp
Transport Direction
N
2 km

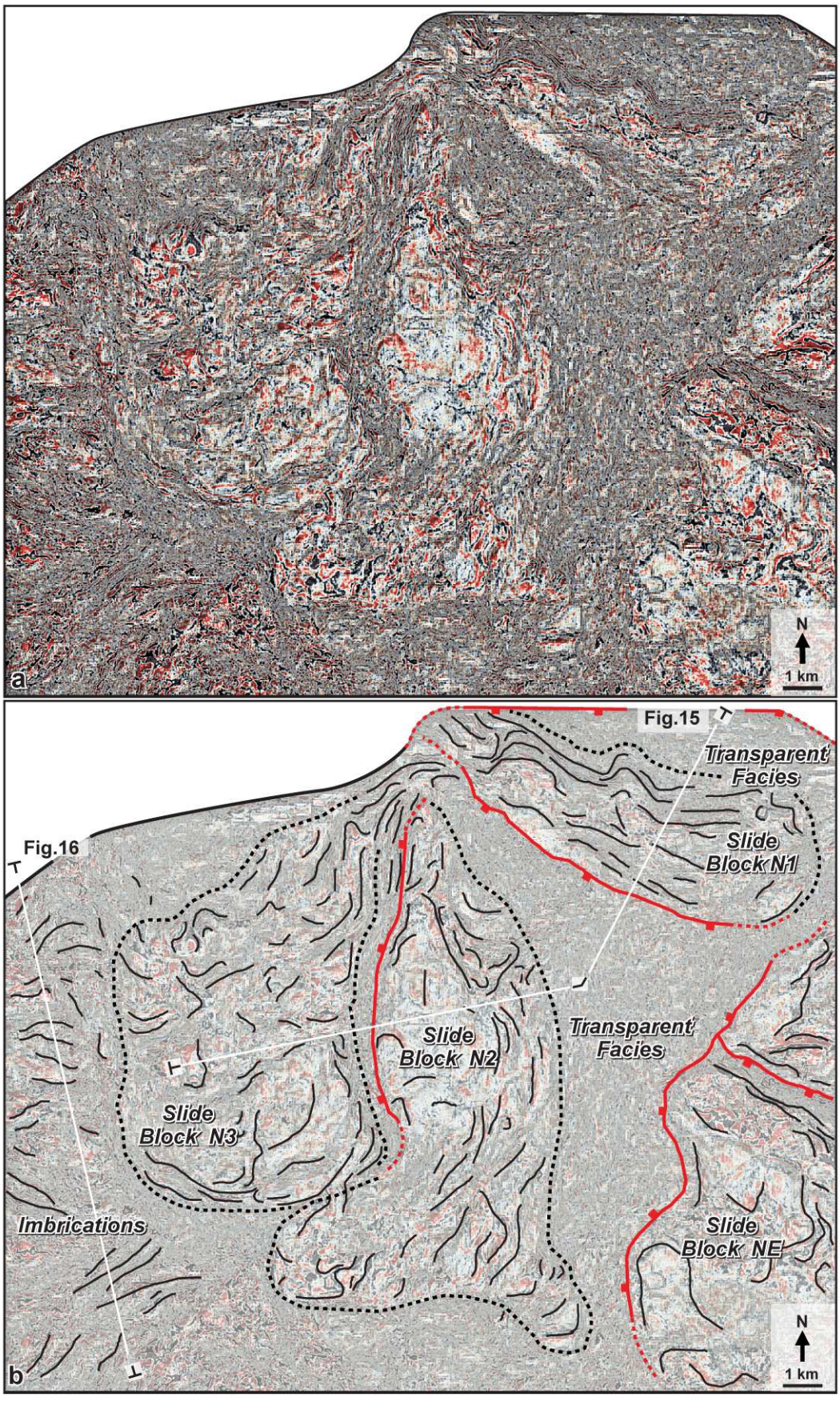
a
N
1 km
b
Fig.15
Fig.16
Transparent Facies
Slide Block N1
Slide Block N2
Slide Block N3
Transparent Facies
Imbrications
Slide Block NE
N
1 km

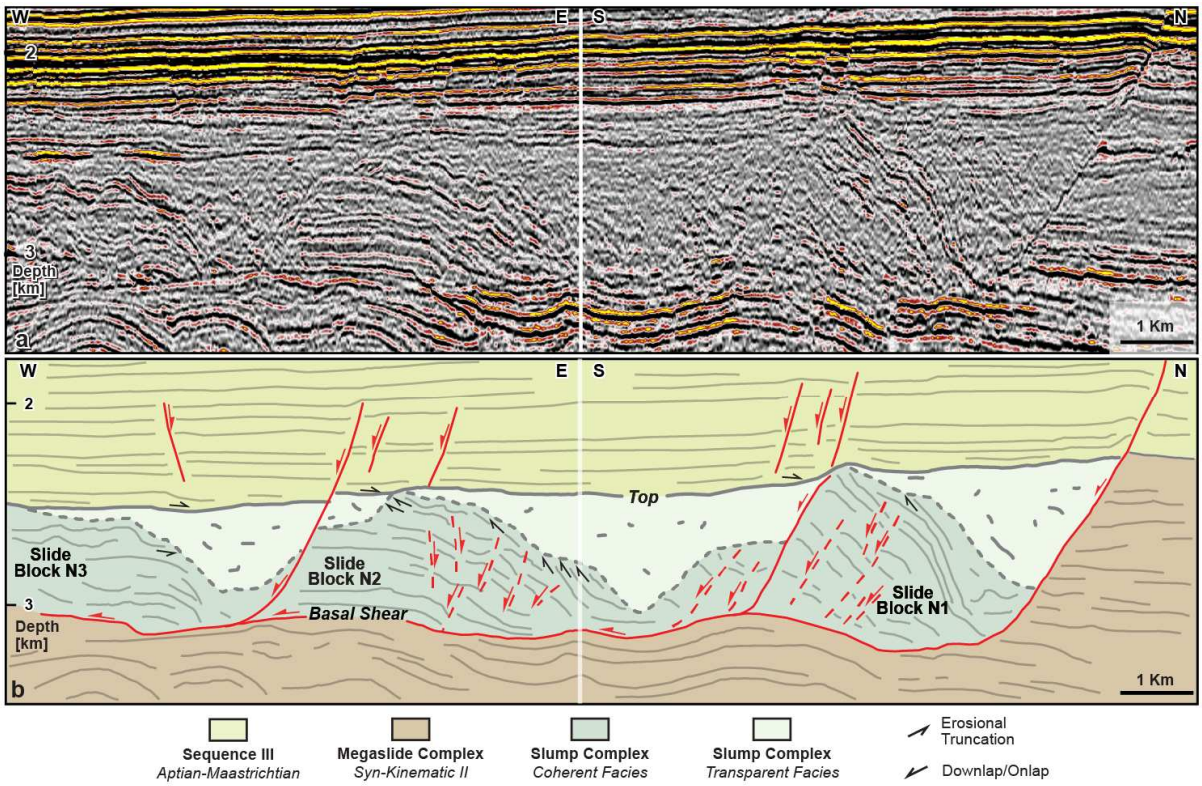

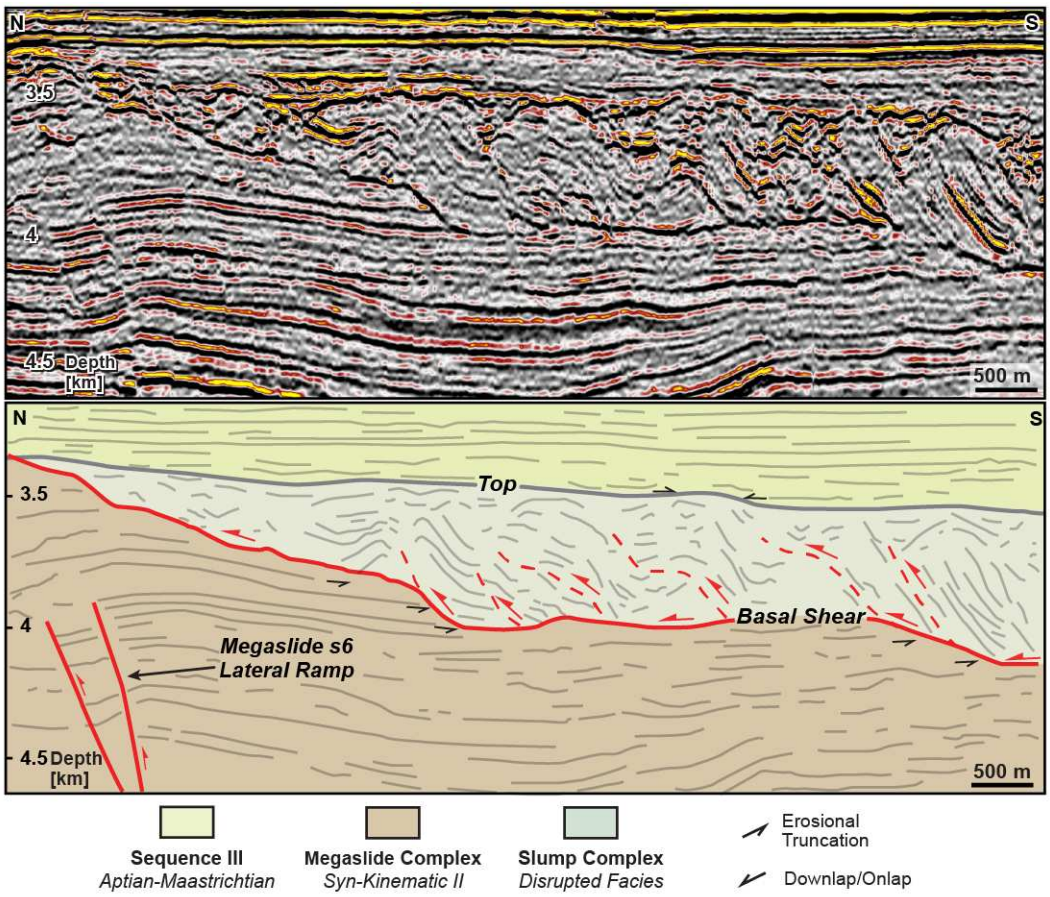

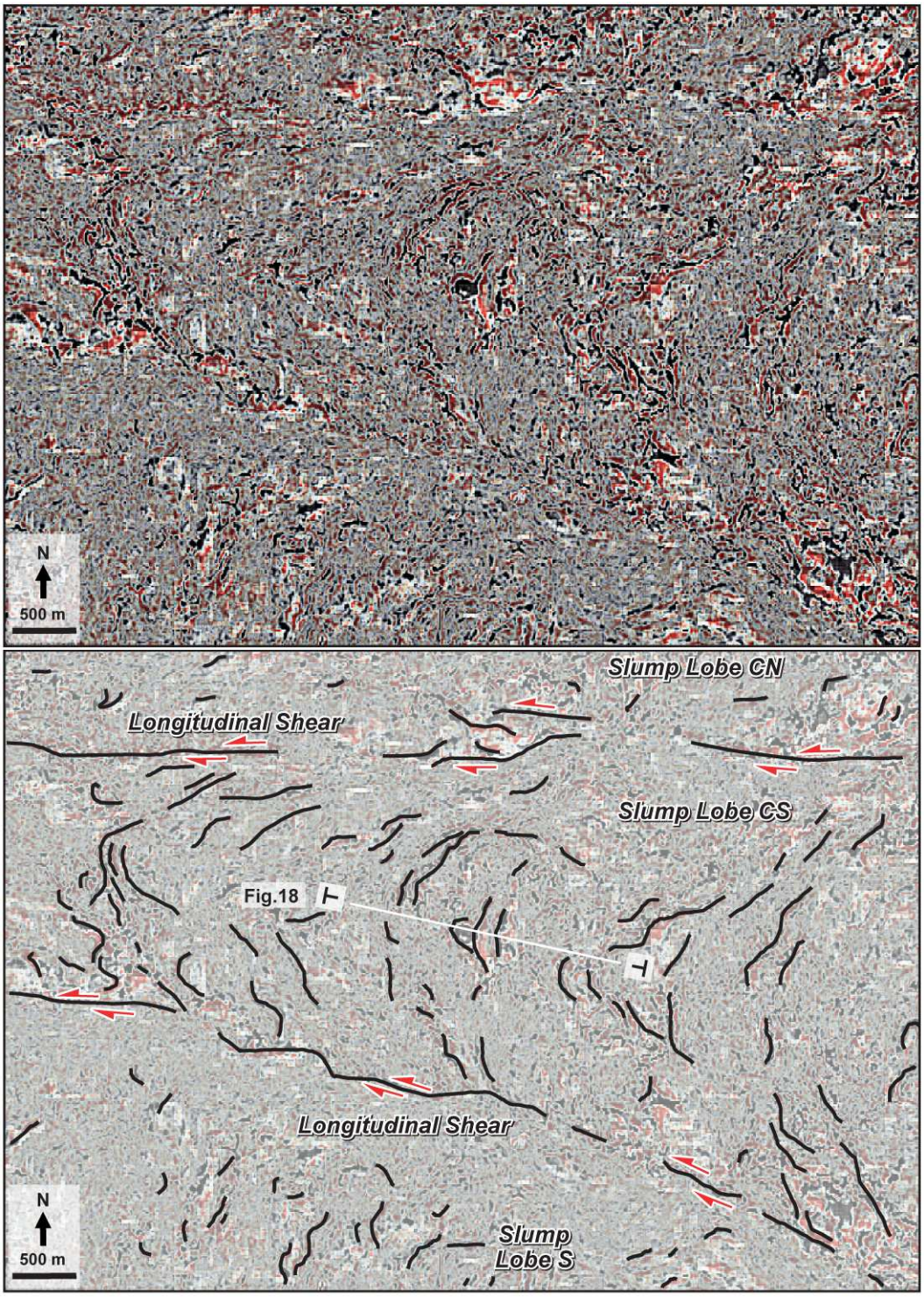
N
500 m
Slump Lobe CN
Longitudinal Shear
Slump Lobe CS
Fig.18
Longitudinal Shear
N
500 m
Slump
Lobe S

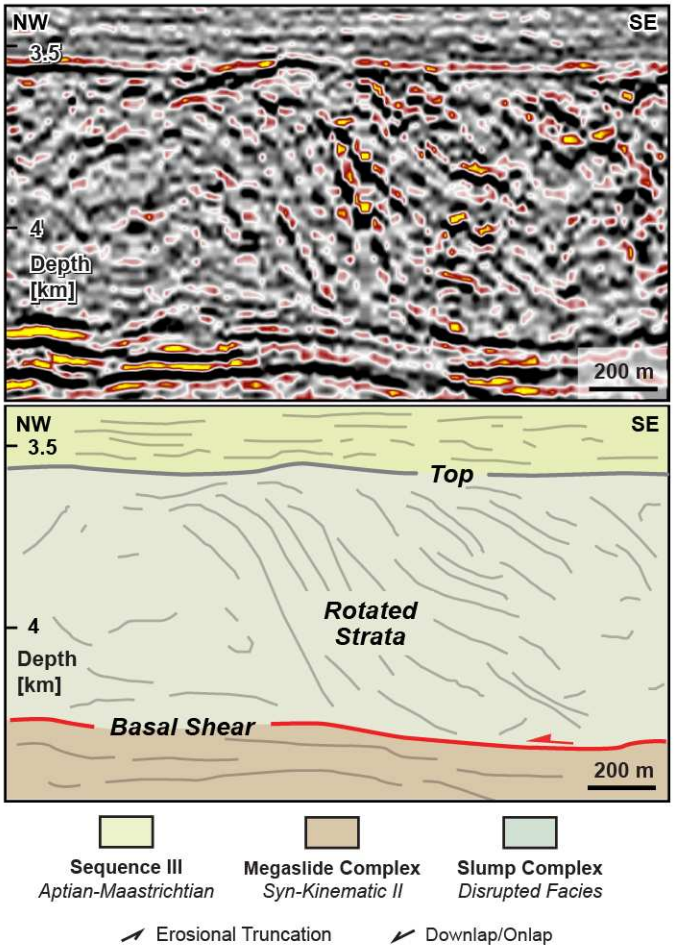

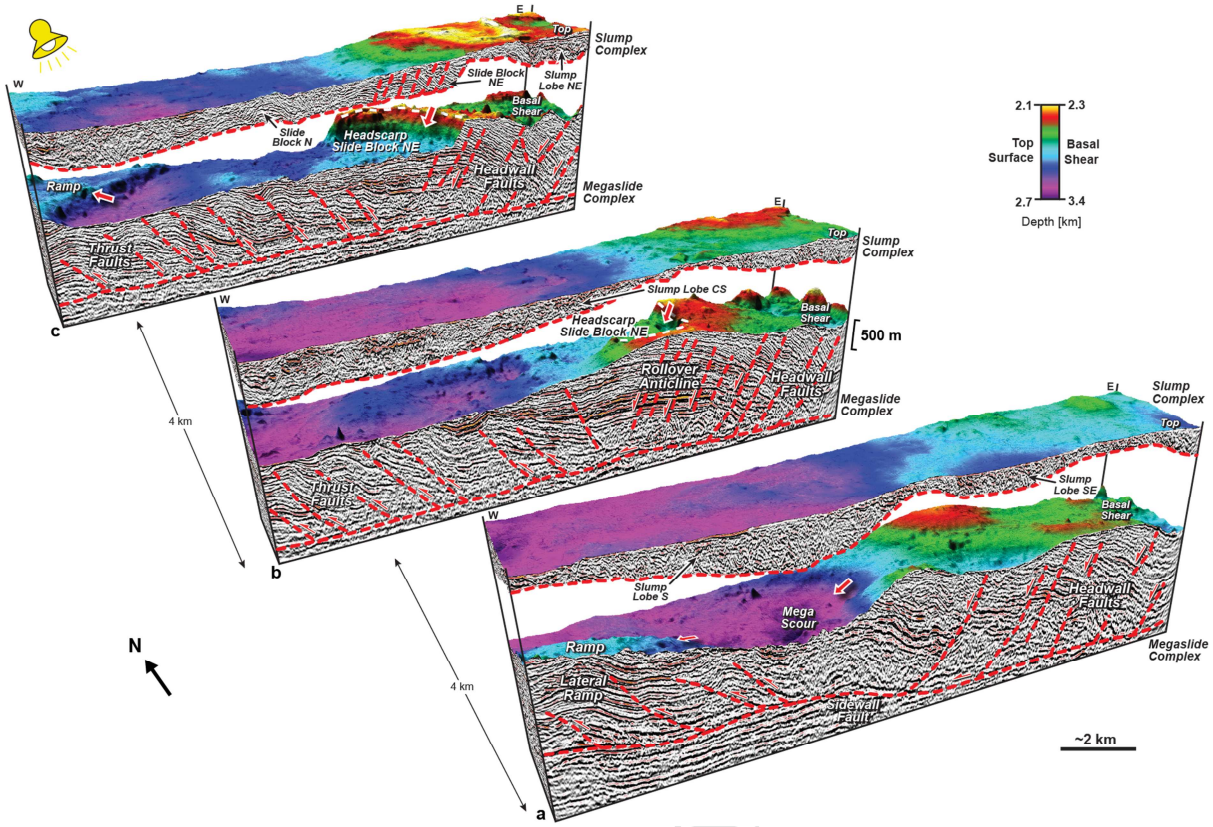
E
W
Top
Slump Complex
Slide Block NE
Slump Lobe NE
Basal Shear
Slide Block N
Headscarp Slide Block NE
Headwall Faults
Ramp
Megaslide Complex
Thrust Faults
c
2.1
2.3
Top Surface
Basal Shear
2.7
3.4
Depth [km]
Slump Lobe CS
500 m
Rollover Anticline
b
4 km
Slump Lobe SE
Slump Lobe S
Mega Scour
Lateral Ramp
Sidewall Fault
a
N
~2 km

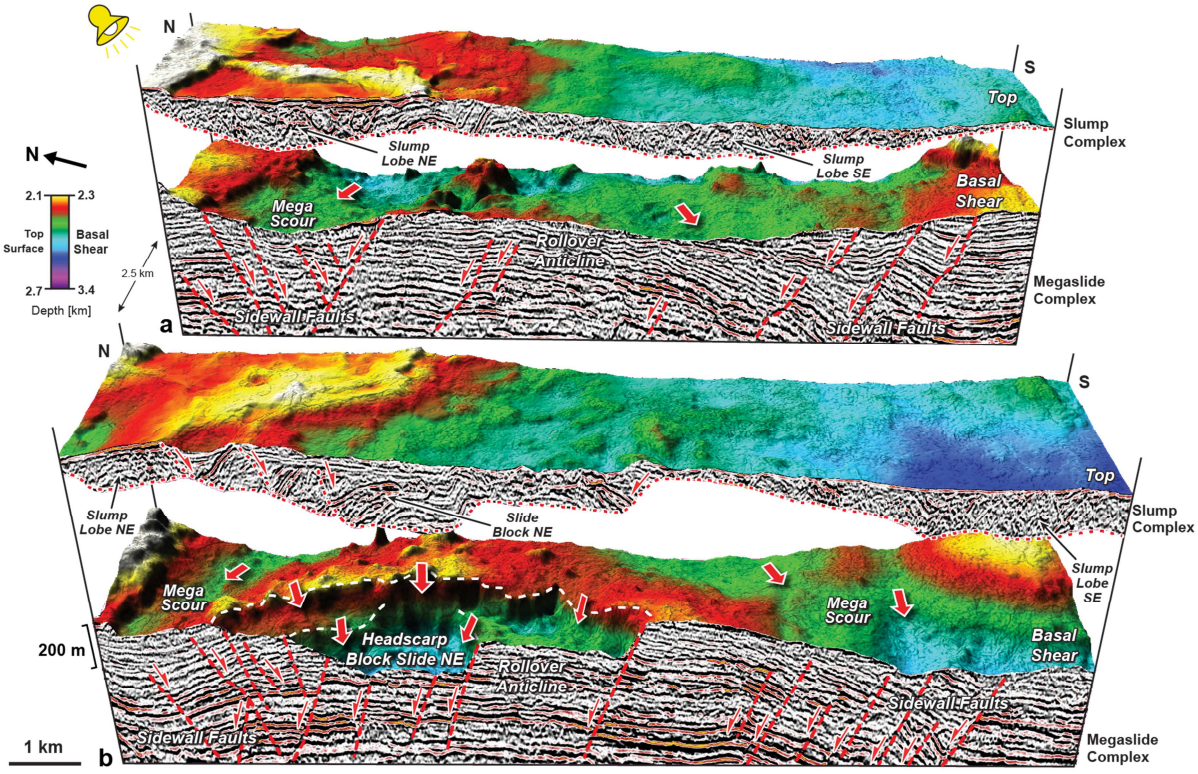

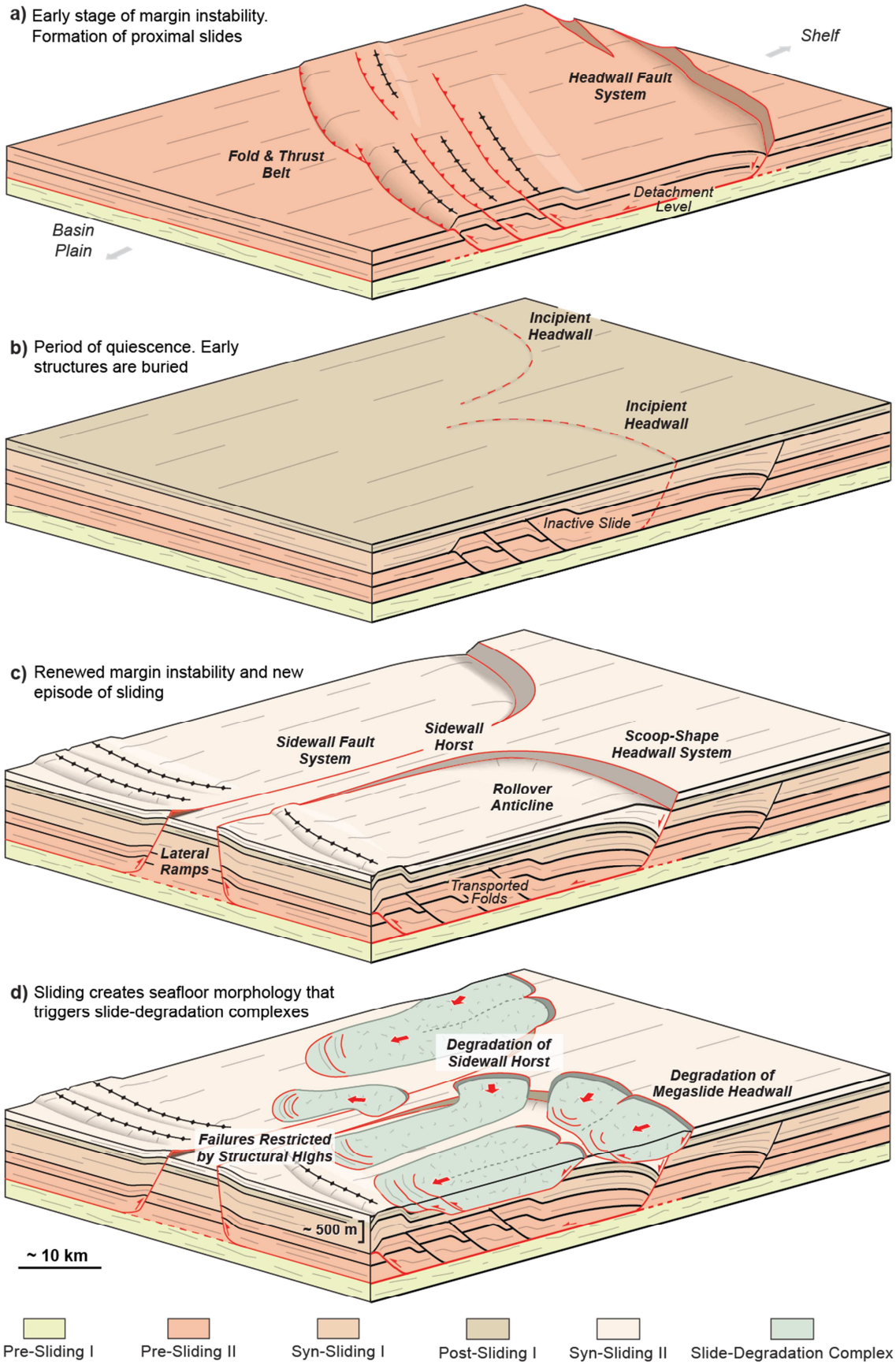
a) Early stage of margin instability. Formation of proximal slides
Shelf
Headwall Fault System
Fold & Thrust Belt
Detachment Level
Basin Plain
b) Period of quiescence. Early structures are buried
Incipient Headwall
Incipient Headwall
Inactive Slide
c) Renewed margin instability and new episode of sliding
Sidewall Fault System
Sidewall Horst
Scoop-Shape Headwall System
Rollover Anticline
Lateral Ramps
Transported Folds
d) Sliding creates seafloor morphology that triggers slide-degradation complexes
Degradation of Sidewall Horst
Degradation of Megaslide Headwall
Failures Restricted by Structural Highs
~ 500 m
~ 10 km
Pre-Sliding I
Pre-Sliding II
Syn-Sliding I
Post-Sliding I
Syn-Sliding II
Slide-Degradation Complex

Seismic Geomorphology of Cretaceous Megaslides Offshore Namibia (Orange Basin): Insights into Segmentation and Degradation of Gravity-Driven Linked Systems.

Nicola Scarselli, Ken McClay and Chris Elders

Highlights

1) 3D seismic geomorphology reveals lateral segmentation of gravity-driven linked systems into km-wide scoop-shaped megaslides

2) Megaslide segmentation provides a variety of hydrocarbon trapping structures

3) Emplacement of megaslides likely to trigger shallow failures with volumes of hundreds of cubic kilometers